CHARACTERIZATION OF ALPHA-PHASE SINTERING OF URANIUM AND URANIUM-ZIRCONIUM ALLOYS FOR ADVANCED NUCLEAR FUEL APPLICATIONS

A Thesis

by

GRANT WILLIAM HELMREICH

Submitted to the Office of Graduate Studies of
Texas A&M University
in partial fulfillment of the requirements for the degree of

MASTER OF SCIENCE

December 2010

Major Subject: Nuclear Engineering

Characterization of Alpha-Phase Sintering of Uranium and Uranium-Zirconium Alloys for Advanced Nuclear Fuel Applications

CHARACTERIZATION OF ALPHA-PHASE SINTERING OF URANIUM AND URANIUM-ZIRCONIUM ALLOYS FOR ADVANCED NUCLEAR FUEL APPLICATIONS

A Thesis

by

GRANT WILLIAM HELMREICH

Submitted to the Office of Graduate Studies of
Texas A&M University
in partial fulfillment of the requirements for the degree of

MASTER OF SCIENCE

Approved by:

Co-Chairs of Committee,	Sean M. McDeavitt
	Lin Shao
Committee Member,	Miladin Radovic
Head of Department,	Raymond Juzaitis

.

December 2010

Major Subject: Nuclear Engineering

ABSTRACT

Characterization of Alpha-Phase Sintering of Uranium and Uranium-Zirconium Alloys for Advanced Nuclear Fuel Applications. (December 2010)

Grant William Helmreich, B.S. Nuclear Engineering; B.A. Chemistry, Texas A&M University

Chair of Advisory Committee: Dr. Sean M. McDeavitt

The sintering behavior of uranium and uranium-zirconium alloys in the alpha phase were characterized in this research. Metal uranium powder was produced from pieces of depleted uranium metal acquired from the Y-12 plant via hydriding/dehydriding process. The size distribution and morphology of the uranium powder produced by this method were determined by digital optical microscopy.

Once the characteristics of the source uranium powder were known, uranium and uranium-zirconium pellets were pressed using a dual-action punch and die. The majority of these pellets were sintered isothermally, first in the alpha phase near 650°C, then in the gamma phase near 800°C. In addition, a few pellets were sintered using more exotic temperature profiles. Pellet shrinkage was continuously measured in situ during sintering.

The isothermal shrinkage rates and sintering temperatures for each pellet were fit to a simple model for the initial phase of sintering of spherical powders. The material specific constants required by this model, including the activation energy of the process, were determined for both uranium and uranium-zirconium.

Following sintering, pellets were sectioned, mounted, and polished for imaging by electron microscopy. Based on these results, the porosity and microstructure of the sintered

pellets were analyzed. The porosity of the uranium-zirconium pellets was consistently lower than that of the pure uranium pellets. In addition, some formation of an alloyed phase of uranium and zirconium was observed.

The research presented within this thesis is a continuation of a previous project; however, this research has produced many new results not previously seen. In addition, a number of issues left unresolved by the previous project have been addressed and solved. Most notably, the low original output of the hydride/dehydride powder production system has been increased by an order of magnitude, the actual characteristics of the powder have been measured and determined, shrinkage data was successfully converted into a sintering model, an alloyed phase of uranium and zirconium was produced, and pellet cracking due to delamination has been eliminated.

DEDICATION

This thesis is dedicated to my grandmother, who first taught me to love learning.

ACKNOWLEDGEMENTS

I would like to thank Dr. McDeavitt for his continuing guidance, support, and encouragement throughout my research.

I would like to thank Dr. D. Cecala and the Y-12 plant in Oak Ridge, Tennessee for providing the depleted uranium used in this project.

I would like to thank Will Sames for his assistance in powder imaging.

I would like to thank Brandon Blamer for his assistance in sample preparation and polishing.

I would like to thank Dr. Guillemette for his expert assistance in SEM imaging.

NOMENCLATURE

TRU	Transuranics
DU	Depleted Uranium
EBR II	Experimental Breeder Reactor II
IFR	Integral Fast Reactor
LVDT	Linear Variable Differential Transformer
SEM	Scanning Electron Microscope
BSE	Backscatter Electron
WDS	Wavelength Dispersive Spectroscopy

TABLE OF CONTENTS

Page

LIST OF FIGURES

Page

Page

Page

LIST OF TABLES

1. INTRODUCTION

Advanced nuclear fuel cycles are currently under development around the world. In many cases, fuel cycle strategies call for the recycling of transuranic (TRU) isotopes for burning in advanced reactor systems. A reactor systems that is especially effective for TRU burning is the metal-fueled fast reactor [1]. Fast reactors driven by uranium alloy nuclear fuels have been operated for over 40 years with injection casting as the predominant fuel fabrication method. However, the low melting points and high vapor pressures of the TRU isotopes of neptunium, americium, and curium make fuel fabrication by melt casting a challenge [2]. Possible solutions to these issues have been proposed and tested [1]; however, alternative means of U-TRU-Zr fuel fabrication have been pursued as well.

Low temperature powder metallurgy methods for the fabrication of U-TRU-Zr alloys are under development at Texas A&M University's Fuel Cycle and Materials Laboratory as a part of the U.S. Department of Energy's Nuclear Energy Research Initiative (NERI). The focus of this particular NERI project is to develop two fabrication methods, alpha-phase sintering and hot extrusion, to produce U-Zr alloys that are either porous or dense at temperatures ranging from 600°C to 800°C. The focus of this thesis is on process development experiments relevant to the alpha phase sintering method. The initial establishment of the uranium powder preparation method and the processing and measurement equipment necessary to perform alpha phase sintering was reported in a previous thesis by D. Garnetti under the direction of S.M. McDeavitt [3]. The research presented in this thesis continues the development of the alpha phase sintering method.

This thesis follows the style of Journal of Nuclear Materials.

Uranium powder for use in sintering studies was generated using a hydride/dehydride process that was based on the method described in [3], but the process variables and methods were improved to increase powder production rates. Optical microscopy and image analysis of the powder produced by this method showed a rough, irregular morphology with a size distribution peak near 40 μm diameter particles.. Uranium alloy powder mixtures were pressed into pellets were with varying compositions, including pure DU, DU-10Zr, and DU-5Zr[1]. Sintering was performed under a variety of conditions, including isothermal alpha phase sintering between 625°C and 660°C, isothermal gamma phase sintering between 795°C and 820°C, and sintering with cyclic phase changes.

The shrinkage associated with sintering for each pellet was measured in situ in real time using a Linear Variable Differential Transformer (LVDT). This system allowed accurate determination of both time and temperature dependencies and calculation of thermodynamic sintering constants, leading to the development of basic sintering models. LVDT measurements were supported by direct physical measurements of pellet dimensions before and after sintering. Based on these measurements, it was found that DU-Zr mixtures sintered more rapidly and to a higher density then pure DU due to enhanced sintering by DU-Zr interdiffusion. In addition, the activation energy for sintering of DU and DU-10Zr were found to be 340 +/-41 kJ/mol and 272 +/-91 kJ/mol respectively.

Following sintering, pellets were sectioned axially, mounted in epoxy, polished, and imaged using SEM. These images were used to analyze the degree of sintering, determine porosity, and identify phases in pellets with alloying constituents. It was found that pellets with low compaction pressures sintered with an inner high density region and an outer low density region due to compaction density gradients; however, increased compaction pressure resulted in

[1] All compositions are presented as weight percent, unless otherwise noted.

uniform density. The sintered phases of DU-Zr pellets were identified to be a uranium rich phase containing small amounts of dispersed zirconium, a zirconium rich phase containing virtually no uranium, and a mixed phase containing both uranium and zirconium. The mixed phase consisted of lamellar $\alpha(DU)+\delta(DUZr_2)$ if the pellet was sintered in the γ-phase, and pure δ-phase if the pellet was sintered in the α-phase.

The following sections present detailed descriptions of the context, methods, results and interpretation of the results for the alpha phase sintering process development. Section 2 describes the scientific background for this thesis, including metal fuel background, sintering theory, and the hydride/dehydride method. Section 3 describes in detail the apparatus and procedures which were used in this research. Section 4 provides the results achieved. Section 5 discusses the significance and meaning of the results. Finally, Section 6 provides a brief summary of the primary results and suggestions for future research on this topic.

2. BACKGROUND

This section presents a summary of the prior experience and physical phenomena relevant to the alpha phase sintering method developed for this thesis. Section 2.1 describes the metal fuels used for fast reactor systems and the injection casting method which has predominantly been used in the past for their fabrication. Section 2.2 describes the basic theory behind sintering, along with a fundamental model for sintering rate. Section 2.3 describes the hydride-dehydride process which was used for the production of uranium powder.

2.1 Uranium Alloys as Nuclear Fuel

2.1.1 Uranium Metal

Uranium metal exists in three distinct phases depending on temperature. The alpha phase is stable at temperatures below 667°C and has a complex orthorhombic structure, as shown in Figure 2-1 [4]. The beta phase is stable between 667°C and 772°C and has a complex tetragonal structure. The gamma phase is stable from 772°C up to the melting point of 1132°C and has a body centered cubic structure [5]. The alpha phase of uranium, which is of primary interest in this work, has a density of 19.04 g/cm^3 at room temperature [6]. The lattice parameters of the alpha phase uranium unit cell, which are more accurate than those shown in Figure 2-1, are a=2.8541Å, b=5.8541Å, and c=4.9536Å [6].

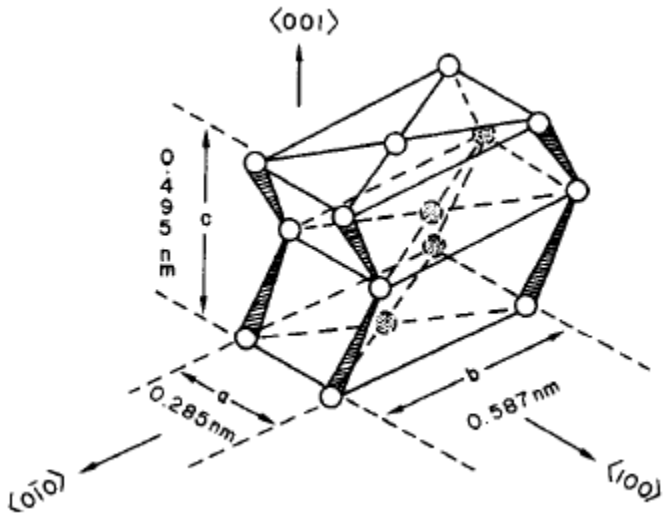

Figure 2-1: Complex orthorhombic structure of alpha phase uranium [4].

2.1.2 Uranium as a Nuclear Fuel

Metallic uranium was an early candidate for use as a fuel form for nuclear energy systems. This fuel form possesses two highly desirable qualities. First, the relatively high conductivity of uranium metal has the potential to minimize the temperature gradient within the fuel. Second, the higher density of uranium metal increases the potential power density available within the fuel. However, it was quickly noted that alpha phase uranium underwent severe swelling and tearing after brief levels of burnup within reactors; the orthorhombic alpha phase allotrope is the dominant microstructure at typical reactor operating temperatures [7]. This effect was caused by the coupling of expansion due to anisotropic fission product accumulation causing uniaxial growth and grain boundary tearing. Further research eventually determined that alloying uranium with small amount of zirconium, molybdenum, titanium and/or other noble metal elements eliminated the anisotropic swelling due to tearing. This enabled the use of uranium alloys as nuclear reactor fuel; however, fission gas bubble formation and gas release is still a performance limiting phenomenon [8]. Although the majority of nuclear reactors currently

utilize oxide fuels, metal fuels are especially viable in fast reactor systems designed to transmute and destroy transuranics (TRUs).

2.1.3 Fabrication of Metal Uranium Fuel

Injection casting is the method most commonly used for fabrication of uranium metal fuels for nuclear reactors, including the manufacture of U-Zr fuel for use at EBR II and in IFR demonstrations. A basic schematic of the injection casting system is given in Figure 2-2. The injection casting process begins by melting liquid U-Zr at approximately 1500°C in a coated graphite melt crucible. The inner crucible wall is typically coated with an oxide mixture consisting of yttria, zirconia, and thorium oxide to minimize interactions between the liquid fuel and the crucible. Quartz injection molds are inserted into the liquid, and pressure is applied to force the fuel into the molds. Once the liquid fuel is injected into the molds and solidified, the molds are destroyed and the cat fuel pins are removed and allowed to cool. The solid fuel is broken away from the molds and machined to the desired final fuel form [9].

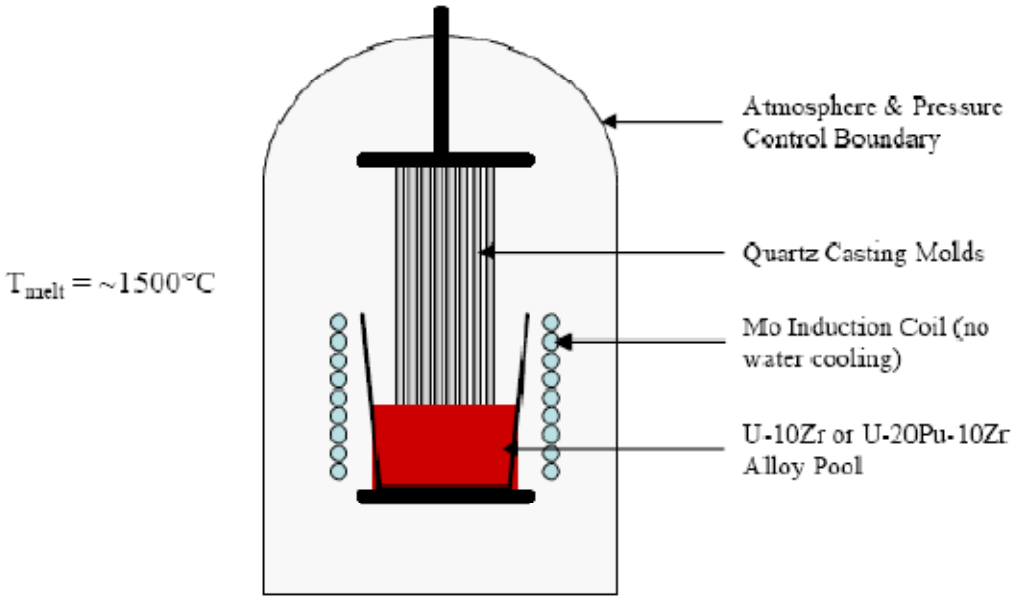

Figure 2-2: Schematic of injection casting system used for U-Zr fuel [3].

Although injection casting is highly effective for the manufacture of U-Zr fuel, it faces potential issues when applied to the fabrication of U-TRU-Zr fuel due to the volatility of some transuranics, most notably americium and neptunium. Figure 2-3 shows the vapor pressures of several transuranics in the temperature range of interest. Initial attempts to fabricate U-TRU-Zr fuel using unmodified U-Zr fabrication procedures resulted in a loss of 40% of the original 2.1wt% Am due to evaporation [2]. Some modifications to the standard U-Zr injection procedures have been shown to significantly reduce transuranic losses, most notably the use of a sealed vessel with a pressurized argon cover gas to reduce Am evaporation and a cold trap to collect the portion which still evaporates. Initial testing of this system with cover gas pressures of 670 Pa and 30 kPa resulted in Am losses of 0.3% and 0.006% respectively [1].

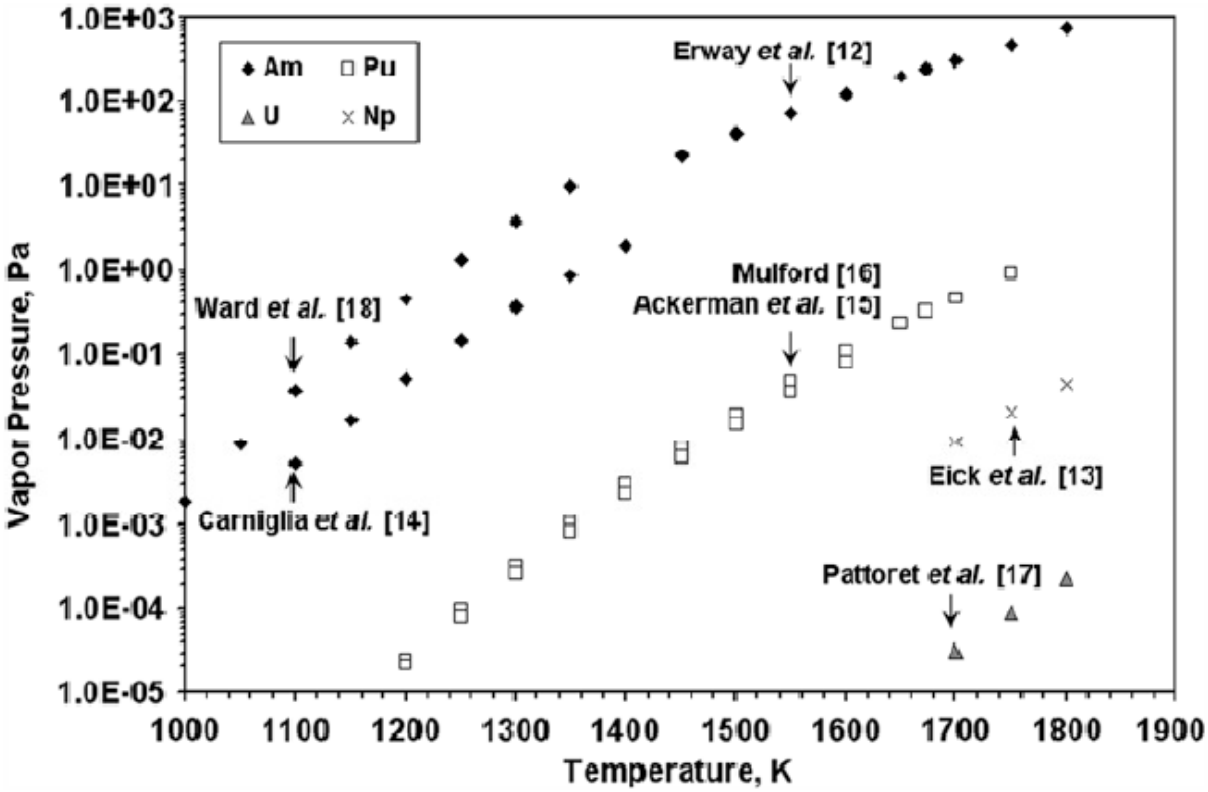

Figure 2-3: Vapor pressures of common transuranics at injection casting temperatures [1].

Previous research performed in the Texas A&M University Fuel Cycle and Materials Laboratory was focused on laying the foundation for an alternative U-TRU-Zr fabrication method based on a powder metallurgy approach with alpha phase uranium sintering [3]; the research described in this thesis continues this work. Sintering processes involving uranium metal are normally performed at temperatures in the gamma phase region, due to the high diffusivity of gamma phase uranium, the dependence of sintering rate on temperature, and for the prevention of oxidation during sintering [10]. However, evidence of low temperature sintering of alpha phase uranium was observed during uranium powder production [11], and during the initial heating regime of experiments focused on gamma phase sintering [10, 12]. The possibility of low temperature sintering is significant for fuel refabrication for TRU burning since the

temperatures used in gamma phase sintering would result in significant evaporative losses of some transuranics, reproducing the challenges encountered with melt-casting.

An initial investigation into the viability of uranium alpha phase sintering was performed as a part of the U.S. Department of Energy's Nuclear Energy Research Initiative (NERI), under the Advanced Fuel Cycle Initiative (AFCI) [3]. Using both live monitoring of pellet shrinkage and SEM imaging, alpha phase sintering was effectively demonstrated for pure uranium samples and for uranium with added zirconium and magnesium [3]. Basic studies of post-sintering porosity were performed; however, rate and thermodynamic analysis were left as potential future work [3].

2.2 Sintering

Sintering is a high temperature phenomenon in which compact powder performs may be densified to form solid materials via various mechanisms that are driven by forces which strive to minimize the overall surface energy within the material. On a practical level, sintering allows for the conversion of fine metallic, ceramic, and polymer powders into solid pieces of a desired shape. Prior to sintering, a typical fabrication process begins with the pressing of powder into a solid compact. This “green” form is then heated to allow bonding and atomic mobility. The typical process variables controlled during sintering include the compaction method, temperature, applied stress, and time. These process variables enable the precise control of the final microstructure and properties of the sintered material [13]. Sintering is commonly used for the fabrication of ceramic nuclear fuel pellets.

2.2.1 Sintering Theory

The microstructure of powder compacts before sintering may be envisioned as a 3-D collection of particles with only point contacts at each particle-particle interface. Due to the large open volume in this system, the overall density of a compact is much lower than the theoretical density of the true solid. In addition, due to the lack of bonding between particles, the strength of the unsintered powder compact is much lower than the strength of the bulk material [14]. As the compact is heated, typically to temperatures at least half of the absolute melting temperature, diffusion within and between particles leads to the formation of broad necks at the original contact points. The growth of necks between particles strengthens the material due to inter-particle bonding. As the sintering process continues, the open pores between particles gradually close, and may eventually be completely filled, resulting in a final strength and density approaching that of bulk material [13].

As studies of the theory behind sintering have progressed, a number of techniques have been developed to quantify the sintering process. The primary measure of sintering used in theoretical models is the neck size ratio, which is defined as the ratio of the neck diameter to the diameter of the particles themselves. Since direct measurement of neck size ratio, especially actively during sintering, is rather difficult, other methods to quantify sintering have been developed. Measurements of density, porosity, shrinkage, and surface area reduction are commonly used, along with measurements of electrical and mechanical properties in some cases. Shrinkage and surface area measurements are particularly useful, as they may be directly related to neck size ratio, and thus are the measurements most commonly used in sintering studies [13].

2.2.2 Sintering Mechanisms and Modeling

The driving factor behind sintering is the reduction of surface energy within the material. The large surface area present in the initial powder compact is gradually reduced as necks form and broaden between particles. Several distinct sintering mechanisms exist but the driving force is identical in each case. The sintering mechanisms may be broadly divided into two categories: surface transport mechanisms and bulk transport mechanisms. Both classes of mechanisms result in neck growth; however, surface transport mechanisms involve the movement of mass along particle surfaces without shrinkage while bulk transport mechanisms involve the movement of mass from within particles to the particle surface with shrinkage [13]. Figure 2-4 demonstrates the difference between surface transport and bulk transport, and shows the various individual mechanisms which contribute to each.

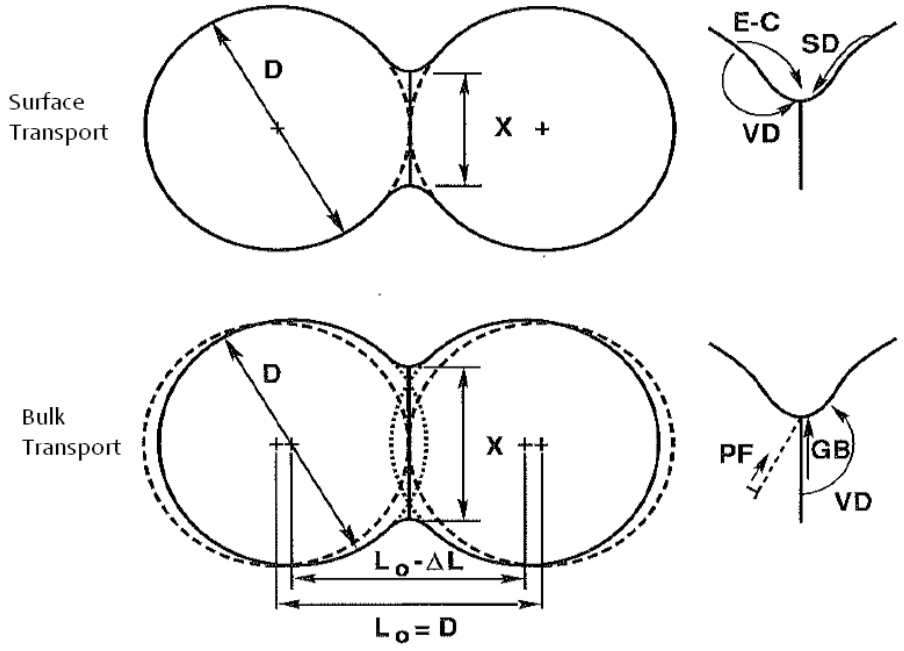

Figure 2-4: Visual representation of surface transport and bulk transport mechanisms, including evaporation-condensation (E-C), surface diffusion (SD), volume diffusion (VD), grain boundary diffusion (GB), and plastic flow (PF) [13].

Surface transport mechanisms include evaporation-condensation and surface diffusion. Evaporation-condensation occurs by the evaporation of surface atoms, transport across open pores, and finally condensation onto a surface. The overall effect of the evaporation-condensation process is the gradual transfer of mass from convex surfaces to concave surfaces, leading to increased necking without a corresponding increase in density. Evaporation-condensation is typically only important as a sintering mechanism at relatively high temperatures and for materials with high vapor pressure near their melting point [14]. Surface diffusion, the second surface transport mechanism, involves the transport of atoms across the free surfaces using surface defects such as kinks. Once again, although surface diffusion contributes to neck growth, it has no effect on density. The required temperature for significant surface diffusion is typically much lower than that of evaporation-condensation; thus, surface diffusion is a common contributor in many sintering processes [13].

Bulk transport mechanisms in sintering include volume diffusion, grain boundary diffusion, and plastic flow. Volume diffusion, which is also called lattice diffusion, is the motion of atoms within each particle by vacancy diffusion. Densification may occur during volume diffusion either by the annihilation of vacancies or by the motion of vacancies toward the boundaries between particles. As vacancies accumulate at particle intersections, layers of atoms between the particles are effectively removed, causing the particle centers to move closer together and broadening the neck between them [13]. Grain boundary diffusion occurs when mass is transported along grain boundaries to the growing bonds between particles. This process is coupled with surface diffusion, which serves to evenly distribute the material as it exits the grain boundary onto the open surface. Since grain boundary diffusion transfers mass from within the particles to the surface, it results in densification of the compact [4]. The final bulk transport

mechanism is plastic flow, in which densification occurs by the motion of dislocations. Plastic flow is inherently limited in its contribution to sintering, because it consumes dislocations as it progresses. Thus, the plastic flow mechanism is typically observed only during initial heating or under applied stress [13].

Theoretical models exist for the kinetics of sintering based on the various mechanisms for mass transport. These models relate the rate of sintering, as measured by neck diameter ratio, to the temperature, time, and particle size, as shown in Equation 2-1 [13].

$$\left(\frac{X}{D}\right)^n = \frac{B_0 \cdot t}{D^m} \cdot e^{\left(-Q/kT\right)} \tag{2-1}$$

Where X is the average neck diameter, D is the average particle diameter, t is the isothermal sintering time, Q is the activation energy of the specific mechanism, k is Boltzmann's constant, T is the absolute temperature, B_0 is a constant dependent on mechanism and material properties, and n and m are integer constants dependent on the sintering mechanism. Since all sintering mechanisms result in neck growth, Equation 2-1 governs both surface and bulk transport mechanisms. Based on the assumption of isotropic sintering, shrinkage may be approximately related to average neck diameter as shown in Equation 2-2 [13].

$$\frac{\Delta L}{L} = \left(\frac{X}{2D}\right)^2 \tag{2-2}$$

Where ΔL/L is the one-dimenstional sintering "strain" associated with isotropic shrinkage. If sintering is not isotropic, then this assumption will lead to a source of internal error as the

uniaxial shrinkage will no longer directly correspond to the degree of sintering. Based on this assumption, Equation 2-1 may be rewritten in terms of shrinkage as shown in Equation 2-3 [4].

$$\left(\frac{\Delta L}{L}\right)^{n/2} = \frac{B_0 \cdot t}{2^n \cdot D^m} \cdot e^{\left(-Q/kT\right)} \qquad (2\text{-}3)$$

Since Equation 2-3 uses shrinkage as its measure of sintering, it is only valid for modeling bulk transport mechanisms. The theoretical values of the integer constants *n* and *m* for each sintering mechanism are given in Table 2-1.

Table 2-1: Integer constants for various sintering mechanisms [13].

Mechanism	Form of Mass Transport	*n*	*m*
Plastic Flow	Bulk	2	1
Evaporation-condensation	Surface	3	2
Volume diffusion	Bulk	5	3
Grain boundary diffusion	Bulk	6	4
Surface diffusion	Surface	7	4

Although each mechanism has specific integer constants, actual experimental results typically show multiple sintering mechanisms over the course of the sintering process. As the relative effect of each mechanism varies, the actual observed values of *n* and *m* will shift gradually over time [13].

2.3 Hydride/Dehydride Processes

The study of uranium powder metallurgy in a laboratory setting necessitates a ready source of high purity, non-oxidized uranium powder. Due to the high susceptibility of uranium metal to oxidation, a hydride/dehydride process for uranium was previously established [3] and improved in this present work to effectively produce fine uranium powders in the quantities required for small scale laboratory research.

2.3.1 Uranium Hydride Formation

When heated to temperatures in excess of 150ºC uranium metal reacts reversibly with hydrogen gas to form UH_3 according to Equation 2-4 [5,15,16].

$$2\,U + 3\,H_2 \leftrightarrow 2\,UH_3 \qquad (2\text{-}4)$$

The density of UH_3 at 25°C is 10.9 g/cm^3, compared to a density of 19.04 g/cm^3 for uranium at 25°C [17]. The large decrease in density following conversion to UH_3 results in a correspondingly large increase in volume. As the reaction proceeds, hydrogen diffuses further into the uranium lattice, eventually causing small pieces of UH_3 powder to spall away from the remainder of the uranium. If the reaction is allowed to continue, it has to potential to fully convert bulk uranium samples into UH_3 powder [8].

The rate of formation of UH_3 depends predominantly on the temperature at which the reaction is performed, the partial pressure of hydrogen, and the presence of contaminants, such as oxygen, which may impede hydrogen diffusion. The temperature for which the hydriding reaction reaches a maximum rate depends somewhat on the partial pressure of hydrogen;

however, the maximum rate occurs at approximately 225°C [5,15]. The hydriding rate as a function of temperature under 580 mmHg of hydrogen is given in Figure 2-5, demonstrating a peak rate at ~225°C.

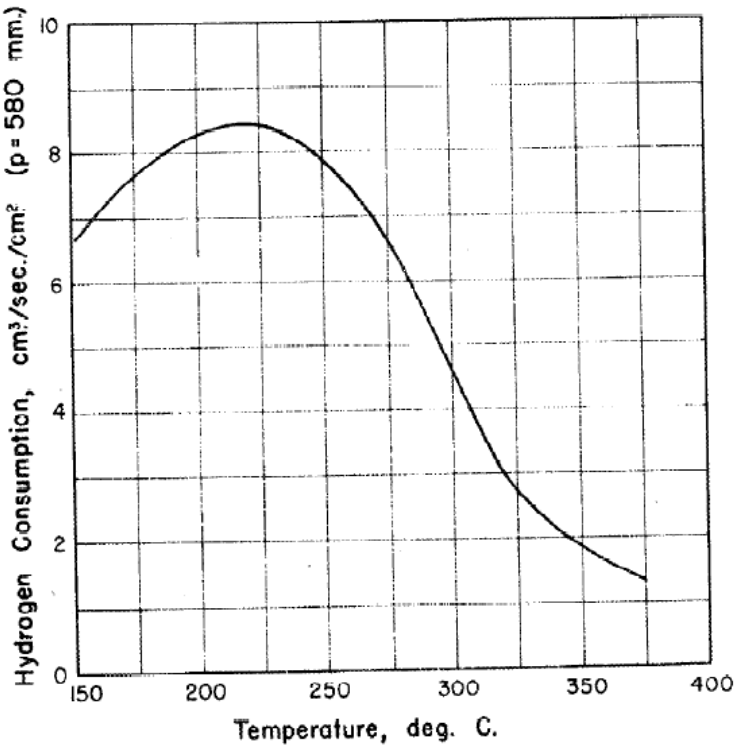

Figure 2-5: Uranium hydride rate of formation at constant pressure [11].

The third condition which strongly affects the rate of hydride formation is the presence of impediments to hydrogen diffusion, most commonly thin oxide films on the bulk uranium. At very low levels of oxygen contamination, a brief induction period may be observed before the hydride reaction commences. At higher levels of oxygen contamination, the oxide barrier to hydrogen diffusion may completely prevent the hydride formation reaction from proceeding [15].

2.3.2 Dehydriding of Uranium Hydride

Due to the reversible nature of the hydride forming reaction, the dehydride step may be performed by increasing temperature and lowering the partial pressure of hydrogen by establishing a rough vacuum [11]. The disassociation of hydrogen leaves behind a fine metal uranium powder, which may then be used for the desired application.

Compared to the hydride process, the dehydride process occurs relatively rapidly. The rate of hydrogen dissociation increases with increasing temperature and lowered hydrogen pressure, reaching a significant rate at temperatures above 300ºC when under vacuum [11]. Although the dehydriding rate may be increased by further increasing temperature, loose sintering of the uranium powder increases with temperature. Thus, if the dehydriding temperature is too high, significant undesired sintering may occur. The rate of hydrogen dissociation as a function of temperature and hydrogen pressure is shown in Figure 2-6.

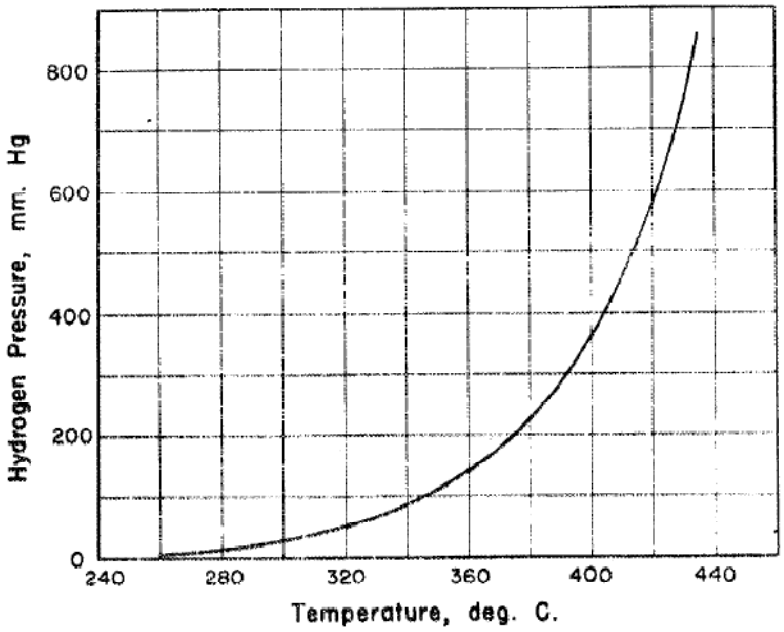

Figure 2-6: Dehydriding rate as a function of temperature and pressure [11].

3. EXPERIMENTAL DESIGN AND PROCEDURES

This section describes the equipment and experimental procedures used in the production of DU powder (3.1), the fabrication of pellets (3.2), the sintering of pellets (3.3), and pellet imaging (3.4). Due to extreme sensitivity to oxygen contamination, the majority procedures performed in this project took place within a large inert atmosphere glovebox with atmosphere recirculation and purification capabilities and a heated furnace well for controlled atmosphere thermal processing. The glovebox is shown in Figure 3-1.

Figure 3-1: Large inert atmosphere glovebox used for handling of pyrophoric uranium powder.

3.1 DU Powder Production

Due to the speed and ease with which uranium metal powder oxidizes, it was necessary to produce uranium metal powder for each test shortly before use within the glovebox shown in Fig. 3-1. Uranium metal coupons, supplied by the Y-12 plant at Oak Ridge National Laboratory, were converted to powder using a uranium hydride/dehydride process, as described in the background section. To increase the volume of powder produced by this process, a specialized set of equipment was designed and developed. The initial system was created by Garnetti [3]; however, modifications and improvements were made.

3.1.1 Acid Washing DU

The hydride formation reaction in Eq. 2-4 is completely inhibited by the presence of surface layers of oxidized uranium. The uranium coupons used for this research were received with oxidized surfaces. The acid washing procedure described here was implemented to remove the majority of this oxide layer, but a very thin oxide film was always present on the metal pieces.

It was determined that the acid wash station should be operated under an inert argon gas atmosphere to minimize re-oxidation of the uranium coupons during and after acid washing. However, it is not possible to perform this water-based operation inside of the inert atmosphere glovebox since the acidic aqueous solution would evaporate rapidly, contaminate the dry atmosphere and degrade the performance of the glovebox purification system. Therefore, the wet chemistry operations were established inside of an the argon-filled glovebag system, as shown in Figure 3-2.

Figure 3-2: Glovebag acid wash station.

The acid washing procedure began with immersion of DU coupons in a beaker containing 25% by volume nitric acid. Light bubbling from the DU was immediately apparent and as the reaction progressed the solution turned light yellow. Visual inspection was used to determine when the oxide layer had been removed, as the coupon changed from dark black when oxidized to a dull gray when clean. Typically the oxide layer would be entirely removed within 5-10 minutes.

Following acid washing, the DU coupons were rinsed with deionized water and then ethanol to clean the surface. The ethanol was allowed to evaporate from the surface before returning the washed DU coupons to the large argon glovebox for hydriding. Due to the potentially volatile result of mixing nitric acid with ethanol, the acid washing station was divided into an aqueous section and an organic section. Strict separation was maintained between the sections to preclude the possibility of an acid-ethanol reaction.

3.1.2 Hydride/Dehydride Process

The hydride/dehydride processing system was designed to be inserted into a 5.08cm (2in) diameter furnace well (Fig. 3-3) located below the large argon atmosphere glovebox and to provide a sealed controllable atmosphere during operation.

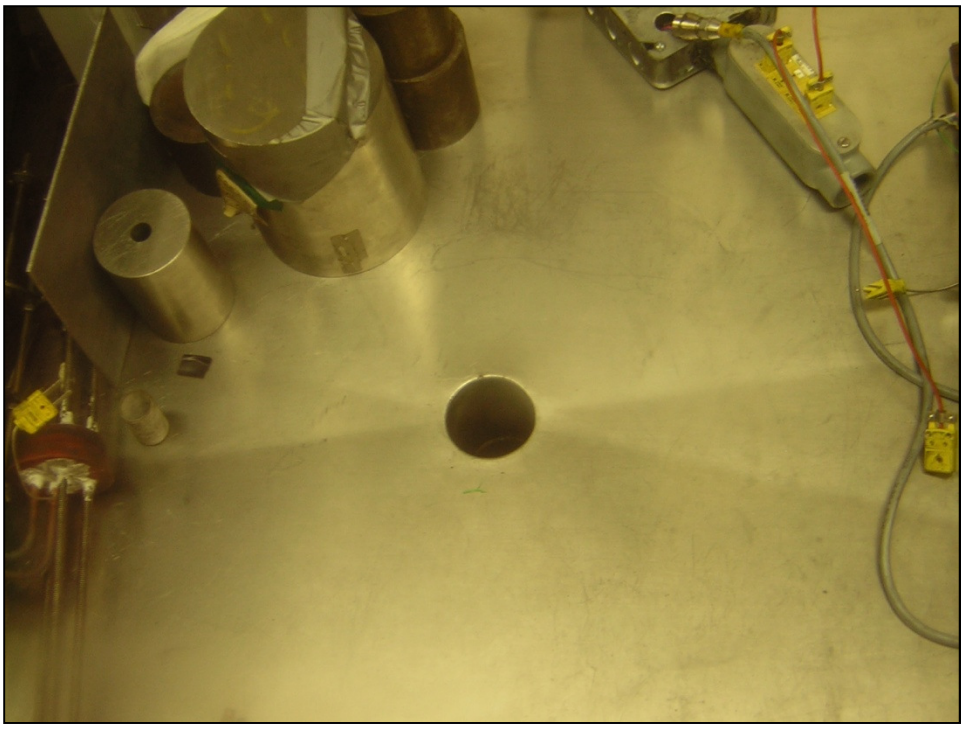

Figure 3-3: Inert atmosphere glovebox furnace well used for powder production and sintering.

The hydride/dehydride well insert (Fig. 3-4) was constructed from three 0.635cm (0.25-in) diameter 316 stainless steel rods with five 304 stainless steel heat shields along their length. A rubber plug was fitted to the top of the steel rods to provide a seal at the top of the furnace. Copper tubing inlet and outlet gas lines (0.635cm dia.) were inserted through the plug, with the inlet line continuing down the full length of the system and the outlet extending only a small amount through the plug. This design produced steady process gas flow through the entire

system. A large yttria crucible was suspended from the bottom of the well insert as the reaction vessel. A fitted piece of coarse stainless steel mesh separated the top and bottom halves of the crucible, allowing solid DU to be positioned in the upper half of the crucible while DU powder fell through to the bottom half as it was produced. Figure 3-5 shows the crucible loaded with several DU coupons before the hydride/dehydride process.

Figure 3-4: Hydride/dehydride well insert used for uranium powder production.

Figure 3-5: DU coupons loaded into yttria crucible for hydriding.

The inlet line of the hydride/dehydride well insert was connected to an Ar-5%H_2 tank with moisture and oxygen traps in line to reduce oxygen contamination. This system delivered the process gas with less than 1 ppm oxygen. The outlet line of the hyrdride/dehydride well insert was connected to an oil bubbler to prevent backflow into the system from the outside atmosphere. The valve system on the outlet line allowed connection to a vacuum pump for evacuation of the furnace well.

The hydride formation reaction was initiated by positioning the loaded hydride/dehydride rig into the glovebox furnace well such that the chamber is sealed from the glovebox atmosphere. The seal formed by the rubber plug at the top of the hydride/dehydride rig was established by a static load distributed on the plug using steel plate with several heavy weights. The furnace well was brought to rough vacuum using the outlet line, then backfilled with Ar-5%H_2 to a gauge pressure of 30 to 50 kpa and a controlled flow rate of 1.4 to 2.4 L/min was established. Once the

system atmosphere was established, the well was heated to 235°C, using a Barnstead 21100 Tube Furnace with attached Eurotherm 211 controller (Fig. 3-6). The temperature and gas flow conditions were maintained for approximately 24 hours to complete the hydriding formation process.

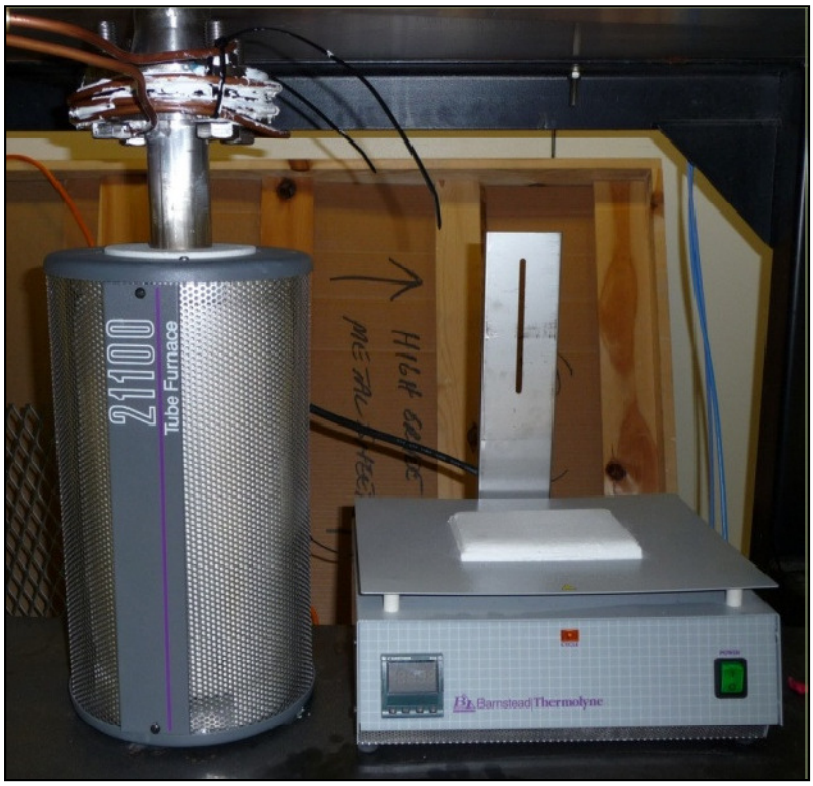

Figure 3-6: Furnace used for hydride/dehydride process.

The dehydride step was initiated immediately following the hydride step. Gas flow through the inlet line was shutoff and the outlet line was used to bring the furnace well to a rough vacuum. The temperature of the furnace was then increased to 325°C. The dehydriding process was observed by monitoring the increase in pressure caused by hydrogen release from the UH_3.

Dehydriding was continued until the pressure reading indicated all hydrogen had been removed from the sample; this was typically accomplished in approximately 30 minutes.

The system was allowed to cool to room temperature following dehydriding before the hydride/dehydride rig was removed. After removal, the DU within the yttria crucible was divided into two portions: 1) solid DU chunks coated with a layer of DU powder resting on the wire mesh and 2) fine DU powder that had fallen through the wire mesh. The powders above and below were normally partially sintered and loose agglomerates of powder were observed. Images of the loosely sintered coupons from atop the wire mesh and the loose powder from below are shown in Figure 3-7 and Figure 3-8 respectively. The large remnant chunks were gently shaken to remove any remaining loose powder and set aside for use in the next powder production run. A typical uranium slug would be fully consumed after three runs. The DU powder which had fallen through the wire mesh was collected and any agglomerates were broken up by light grinding with a steel mortar and pestle. The yttria crucible could be loaded with approximately 80 grams of DU coupons and approximately half of the loaded DU was typically converted into powder each run, resulting in an output of approximately 40 grams of powder per hydride/dehydride run.

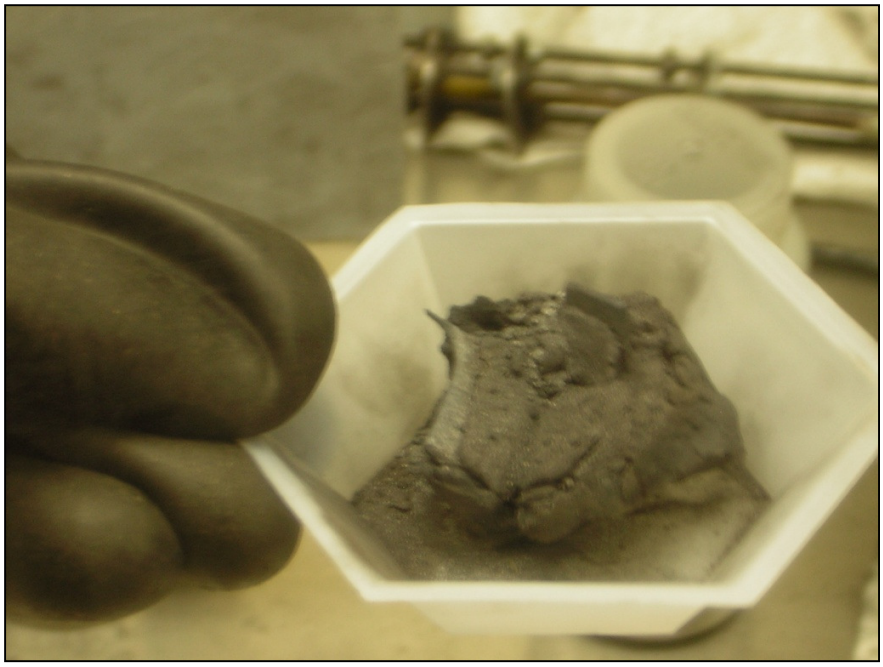

Figure 3-7: Loosely sintering DU coupons coated in powder following dehydriding.

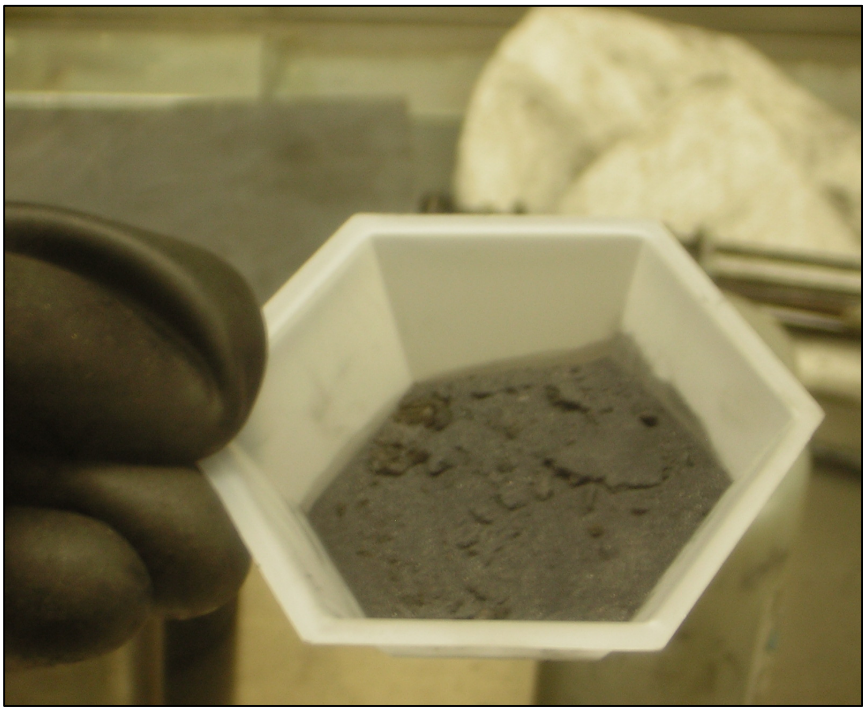

Figure 3-8: DU powder produced by the hydride/dehydride process.

3.1.3 Powder Characterization

The powder produced by the hydride/dehydride process was characterized using optical microscopy. To allow transport of pyrophoric DU powder outside the inert atmosphere glovebox, and Atmospheric Containment Vessel (ACV) was constructed. The ACV, shown in Figure 3-9, consisted of a 1.8 (0.75 in) cm tall, 6.35 cm (2.5 in) diameter nipple with a flange on either side. The top flange had a quartz viewing crystal built in to allow for imaging of powder within the ACV.

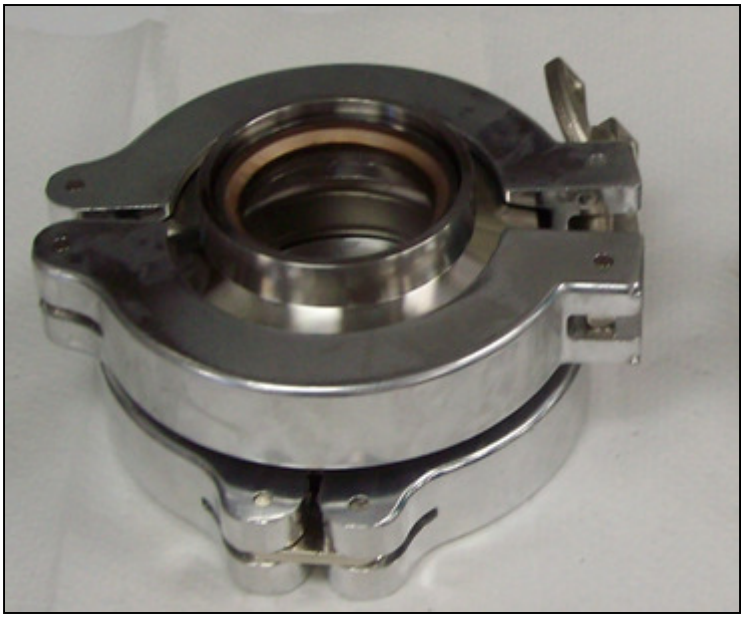

Figure 3-9: Atmospheric Containment Vessel (ACV) used for powder transfer.

The ACV was loaded with DU powder within the large inert atmosphere glovebox. The amount of powder used was very small, as it was desired that each particle be isolated from the others. Once loaded, the ACV was sealed and removed from the glovebox for imaging with a Hirox KH-1300 Digital Microscope, shown in Figure 3-10. Images from multiple powder

production runs at 800x magnification were used with ImageJ grayscale analysis to determine the size distribution of particles.

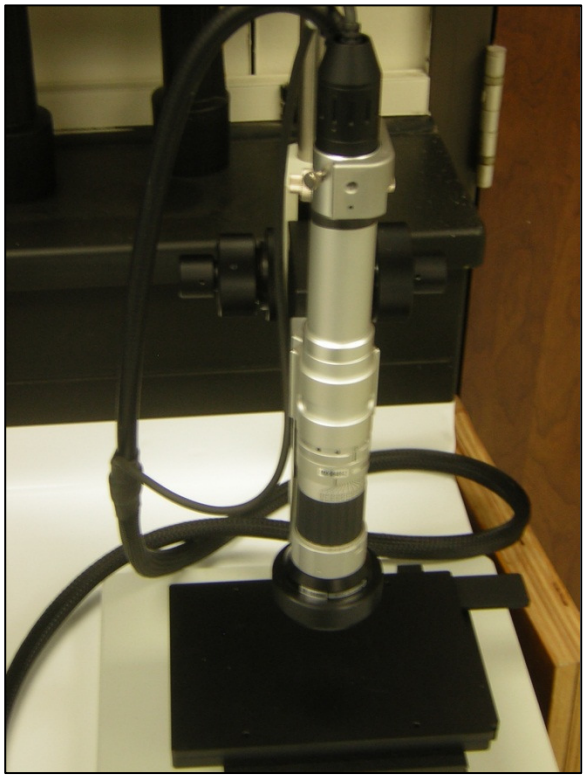

Figure 3-10: Hirox KH-1300 Digital Microscope used for powder imaging.

3.2 Pellet Fabrication

This section reviews the essential steps in converting DU powder into complete sample pellets, including mixing in additive powders (3.2.1), pressing powders into compacts (3.2.2), and sintering green compacts into solid pellets (3.2.3). All processes described in this section were performed in the large inert atmosphere glovebox.

3.2.1 Mixing Powders

For pellets containing zirconium in addition to DU, mixing of the powders was the first step in pellet formation. The DU powder used was produced by a hydride/dehydride process as

described in Section 3.1. The zirconium powder used was 99.7% pure and 325 mesh, supplied by Cerac Inc. Specialty Inorganics.

The mixing procedure started by weighing the DU powder in a small glass jar on a Mettler Toledo AL204 scale, accurate to +/- 0.0005g. A calculation was then performed to determine the total weight which was required to obtain a given weight percent of additives. The additive powders were slowly added to the glass jar while still on the scale, until the appropriate total weight was achieved.

Once all desired powders had been combined, the lid was securely fastened to the glass jar. The jar was shaken with irregular motions for at least ten minutes to ensure thorough homogenization of all constituents.

3.2.2 Compact Pressing

A dual-action punch and die was used to convert loose powder into compacts. The die was fabricated from 303 stainless steel and had a diameter of 0.95 cm (0.375 in). The punches were fabricated from H13 tool steel and were incrementally turned down until they just fit through the die. The punches were heat treated to increase their hardness and prevent bending under pressure.

Powder was loaded into the die by pouring through a funnel while the bottom punch was in place, as shown in Figure 3-11. Once the powder had been loaded, the top punch was inserted. The punch and die were then inserted into a hydraulic Carver Laboratory Press Model C, as shown in Figure 3-12. The compacts were pressed with a load of 44.5 kN (10,000 lbf) for a period of 15 seconds, equating to a pressure of 624,000 MPa.

Figure 3-11: Loading powder into dual-action punch and die for compaction.

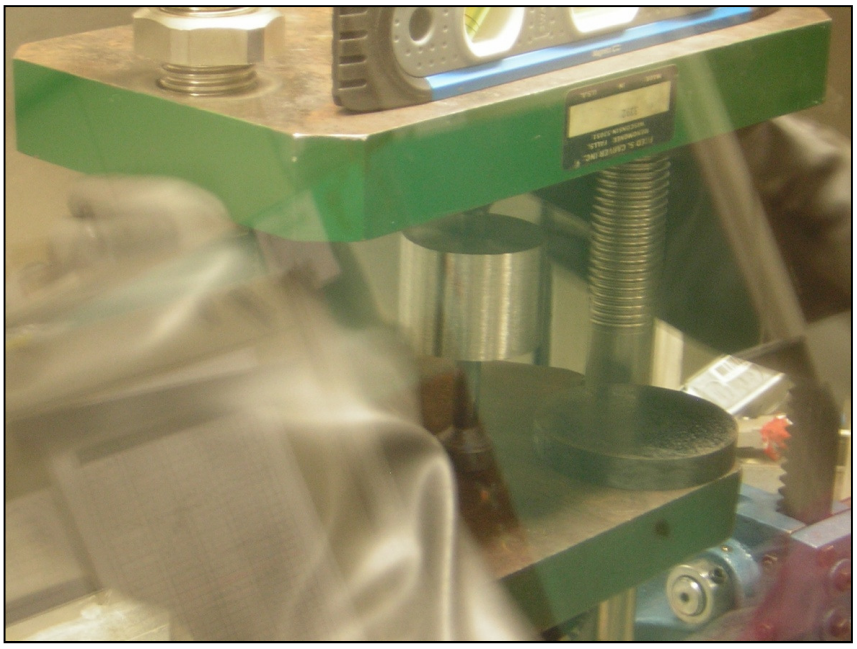

Figure 3-12: Pressing powder compact using hydraulic press.

Following pressing, compacts were removed and pre-sintering measurements of weight, height, and diameter were taken. Five measurements of each value were taken to provide an accurate average result.

3.2.3 Pellet Sintering

The sintering apparatus used in this research was similar to the hydride/dehydride rig described in Section 3.1. The body of the sintering apparatus consisted of three 316 stainless steel rods held together by a series of 304 stainless steel heat shields. The top of the sintering apparatus was a large disk, broad enough to overlap the furnace well opening and suspend the entire apparatus. Powder compacts to be sintered were loaded into a small yttria crucible, which fit into a small cup at the bottom of the sintering apparatus. Figure 3-13 provides an image of the sintering apparatus.

.

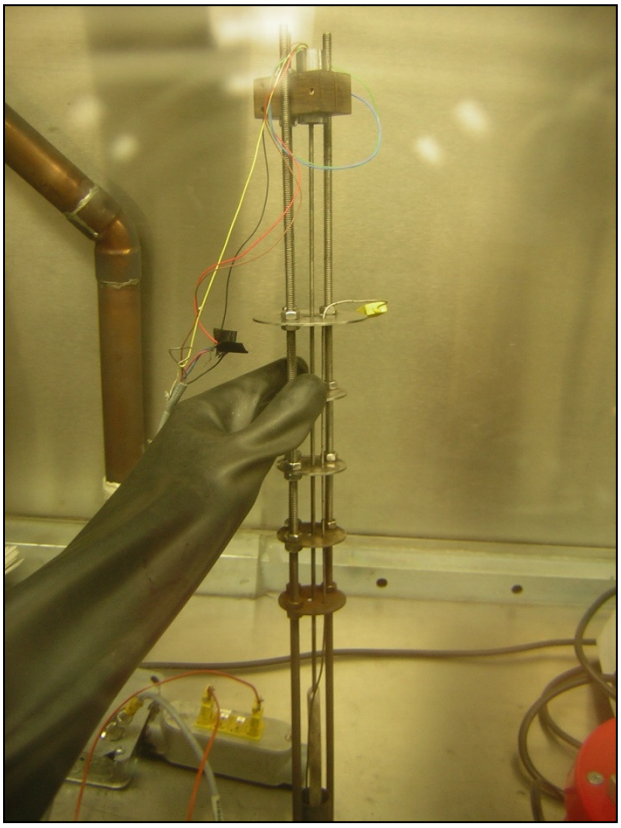

Figure 3-13: Photograph of the sintering apparatus showing LVDT at top and sample holder at bottom.

In situ measurements of the sintering process were provided by a thermocouple inserted into the yttria crucible and a Linear Variable Differential Transformer (LVDT). The magnet within the LVDT was coupled to the sintering pellet by means of a long steel rod which sat on the top of the pellet. As shrinkage occurred in the pellet due to sintering, the rod and magnet shifted in the LVDT sleeve, providing an electrical output. A yttria sleeve was added to the bottom end of the rod to prevent contact, and possible interactions, between the pellet and the steel rod. Both the LVDT and the thermocouple outputs were processed using a National Instruments USB-6210 system, which in turn output to Labview SignalExpress.

Once compacts were loaded into the sintering apparatus, they were heated to temperature in the same furnace well used for the hydride/dehydride process in Section 3.1. Several forms of temperature profiles were used to provide multiple perspectives on the sintering process. Some pellets were sintered isothermally at temperatures in the α-phase of uranium, then sintered isothermally at temperatures in the γ-phase of uranium. Some pellets were sintered exclusively in the α-phase of uranium. Finally, some pellets were sintering with cyclic temperature changes to induce internal stresses, promoting plastic deformation.

After sintering was complete, the measurements performed before sintering to determine height, diameter, and mass of the pellet were repeated. Once again, each measurement was made five times to provide an accurate average.

3.3 Pellet Imaging

After sintering, pellets were sectioned, polished, and SEM imaged. Pellets were sectioned axially using a LECO VC-50 Diamond saw. The pellet samples were then mounted in epoxy with the freshly sectioned face exposed. A Buehler Minimet-1000 was used to polish the exposed face of each pellet, starting with coarse 400 grit abrasive paper and finishing with 1 micron diamond paste.

After polishing was complete, pellets were imaged using a Cameca SX50 Electron Microprobe equipped with a PGT Energy Dispersive X-ray (EDS) system. In addition to traditional SEM images, the EDS system was used to identify the elemental compositions of various phases which were observed.

3.4 Sintering Calculations

The ultimate goal of the experiments performed was to quantify the sintering rates and mechanism by identifying the constants associate with the German model presented in Eq. 2-3 . To accomplish this goal, basic calculations and analyses of the raw data were required. The equations used to model sintering rates are described in Section 2.1.3. During isothermal sintering, the exponential term becomes constant, simplifying Equation 2-3 to Equation 3-1.

$$\frac{\Delta L}{L} = C \cdot t^{2/n} \tag{3-1}$$

Equation 3-1 may be further simplified for modeling by taking the logarithm of each side, producing Equation 3-2.

$$Ln\left(\frac{\Delta L}{L}\right) = Ln(C) + \frac{2}{n}Ln(t) \tag{3-2}$$

In this form, *n* may be easily calculated by finding the slope of a log-log plot of shrinkage versus time. This method was applied to each pellet which was isothermally sintered. An initial guess for the isothermal sintering starting time was determined by the approximate point at which temperature stabilized for each pellet. This starting time was then modified slightly in each direction to determine the point at which the greatest degree of linearity occurred in the log-log plot of shrinkage vs. time. The validity of this technique is demonstrated by the divergence from linearity to a curve if the starting time of the model is shifted forward or backward.

Once *n* was determined for several pellets of the same composition at different isothermal sintering temperatures, the data from the pellets was combined to form an Arrhenius plot. Once

again starting from Equation 2-3, if time is set to be constant across multiple temperatures, Equation 3-3 results.

$$\frac{\Delta L}{L} = C \cdot \left[\exp\left(-{}^{Q}/_{kT}\right)\right]^{2/n} \tag{3-3}$$

In a similar fashion to Equation 3-1, taking the logarithm of both sides of Equation 3-3 results in a form which is much simpler to analyze, as shown in Equation 3-4.

$$Ln\left(\frac{\Delta L}{L}\right) = Ln(C) - \frac{2 \cdot Q}{n \cdot k} \cdot \frac{1}{T} \tag{3-4}$$

Based on Equation 3-4, Q for the process may be determined from the slope of a plot of the logarithm of shrinkage at a specific time versus inverse temperature, if n is already known. The key to this analysis was the selection of the specific sintering time to use. Since the greatest variation typically occurred during the initial and final stages of sintering, the times selected were from the middle stage.

4. RESULTS

This section describes the characterization of uranium powder produced by the hydride/dehydride process (4.1) and the sintering of uranium and uranium alloys under various conditions (4.2).

4.1 Uranium Powder Characterization

Images of uranium powder generated by the hydride/dehydride process were taken using a Hirox KH-1300 Digital Microscope and analyzed using ImageJ software. The images used were taken at 800x magnification. Images containing a total of nearly 6000 particles were used, taken from powder samples from three separate hydride/dehydride runs. These images consistently showed that the powder consisted of many small particles with some larger particles and aggregates. The individual particles were irregularly shaped with rough surfaces. An example image showing these characteristics is given in Figure 4-1.

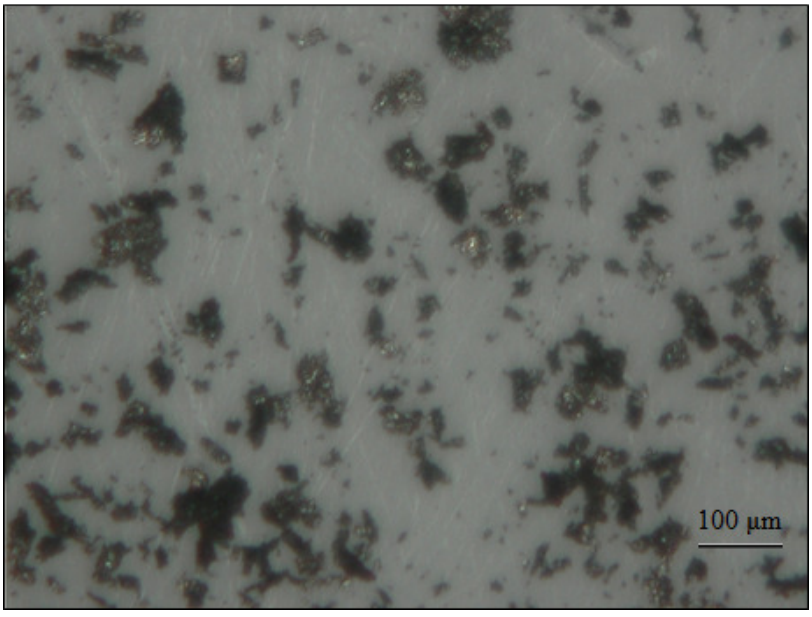

Figure 4-1: Image of uranium powder produced by hydride/dehydride process.

The particle size distribution, as shown in Figure 4-2, was determined in terms of both number density and volume density, based on a simplifying assumption of approximately spherical particles.

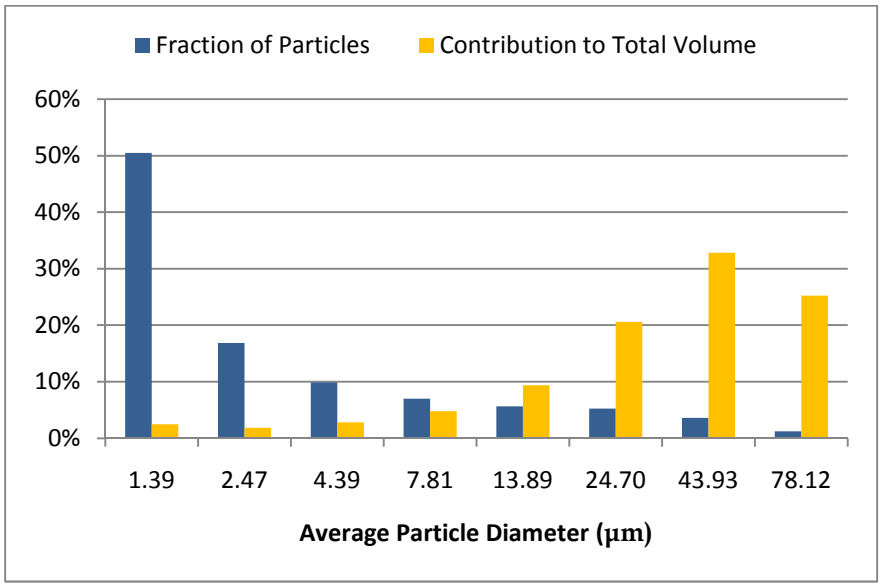

Figure 4-2: Size distribution of uranium powder produced via hydride/dehydride process.

4.2 Uranium and Uranium Alloy Sintering

The pressed uranium pellets were sintered under a wide variety of conditions. Variations in zirconium content, sintering temperature, and temperature profile were used to analyze the sintering process.

4.2.1 Isothermal Sintering of Uranium

The first set of sintering experiments performed used pure uranium pellets with isothermal sintering temperatures. Each pellet was sintered for several hours in the alpha phase, then for several hours in the gamma phase. A total of eight pellets were manufactured, with five

successful sintering runs. A description of each pellet and its sintering conditions is given in Table 4-1.

Table 4-1: Summary of isothermally sintered uranium pellets.

Pellet #	Powder Source	Contents	α-Temperature	γ-Temperature	Green Density	Sintered Density
1	H/dH Run 1	DU	630 °C	N/A	N/A	N/A
2	H/dH Run 1	DU	N/A	N/A	N/A	N/A
3	H/dH Run 2	DU	655 °C	N/A	N/A	N/A
4	H/dH Run 2	DU	655 °C	831 °C	53.95%	57.87%
5	H/dH Run 3	DU	643 °C	820 °C	47.21%	49.88%
6	H/dH Run 3	DU	634 °C	809 °C	46.68%	50.46%
7	H/dH Run 3	DU	659 °C	834 °C	47.17%	51.22%
8	H/dH Run 3	DU	651 °C	826 °C	48.20%	51.97%

Pellet 1 was pressed with a force of 66.8 kN (15,000 lbs), corresponding to 936,000 MPa. The press was raised to this force a total of eight times, and each time the pressure was allowed to bleed naturally. Upon removal from the die, several small pieces of the pellet chipped off one of the faces, indicating excessive stresses within the pellet and possible binding to the inner walls of the die. In spite of this, the pellet was sintered at 630ºC for 24 hours. The LVDT output showed no signs of sintering.

Pellet 2 was pressed with a sustained force of 44.5 kN (10,000 lbs), corresponding to 624,000 MPa, for 30 minutes. Significant portions of the pellet crumbled upon removal from the die, even more so than Pellet 1. Due to the lack of success in sintering Pellet 1, no attempt was made to sinter Pellet 2.

Pellet 3 was pressed with a force of 44.5 kN (10,000 lbs), corresponding to 624,000 MPa, for 15 seconds, after which the pressure was allowed to bleed off naturally. The pellet did not

crumble upon removal from the die; therefore, this pressing regime was used for all future pellets. An image of Pellet 3 as pressed is shown in Figure 4-3. Pellet 3 was sintered at 655ºC for 24 hours; however, shrinkage was only observed during temperature ramping from 300ºC up to the isothermal hold temperature. The lack of isothermal sintering in Pellet 3 was attributed to the source powder used. Pellet 3 was comprised entirely of powder which had loosely sintered during the dehydride process. These chunks were broken and ground with a steel mortar and pestle, then mechanically agitated in a small steel vial with a steel ball bearing; however, the resulting particle size was still likely larger than that of the loose powder. Due to this, all future pellets were fabricated using only the loose powder.

A red powder was observed on the top of the pellet after sintering, as shown in Figure 4-4. This powder was likely an iron-bearing reaction product generated by hot contact between the steel LVDT rod and the sample. All subsequent sintering experiments were performed with a ceramic sleeve over the LVDT rod to prevent this.

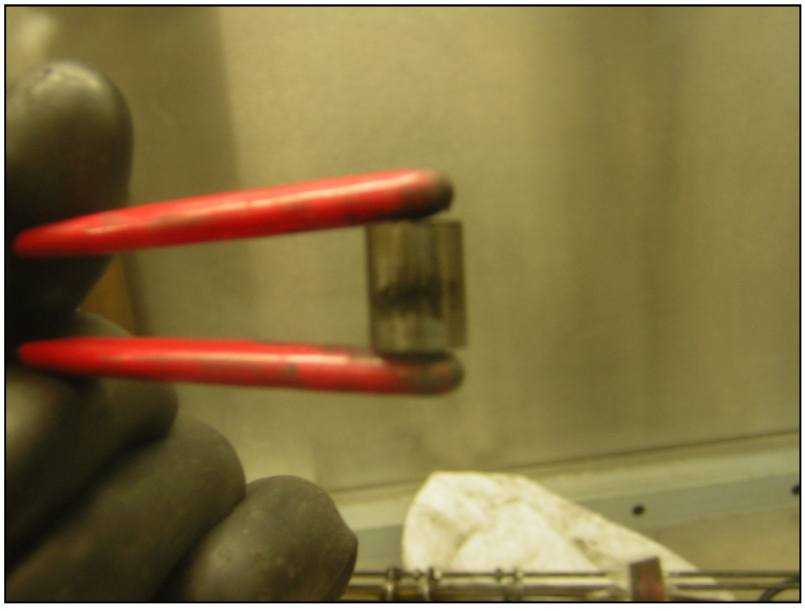

Figure 4-3: Pellet 3 as pressed, before sintering.

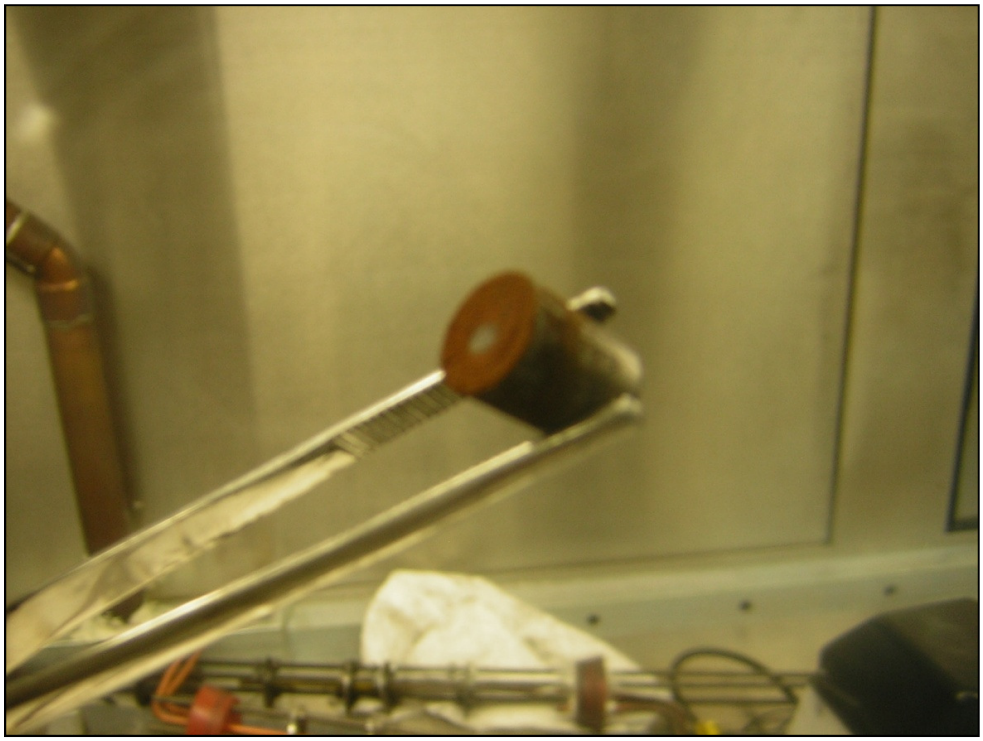

Figure 4-4: Pellet 3 after sintering, with red U-Fe powder formation.

Pellet 4 was the first fully successful isothermal sintering experiment performed. Like Pellet 3 and all following pellets, Pellet 4 was pressed with a force of 44.5 kN (10,000 lbs), corresponding to 624,000 MPa, for 15 seconds, after which the pressure was allowed to bleed off naturally. Pellet 4 was sintered for 4 hours at 655ºC (α-phase), then for 11 hours at 831ºC (γ-phase). A ramp rate of 5ºC/min was used during heating, and a rate of 2ºC/min was used during cooling. An Image of Pellet 4 after sintering is given in Figure 4-5. The light blue coating on the side of the pellet after sintering was likely due to the presence of trace contaminants in the system.

Figure 4-5: Pellet 4 after sintering.

The LVDT data for Pellet 4 exhibited an initial shrinkage during heating similar to that observed for Pellet 3. However, sustained shrinkage was observed at the each of the isothermal holding temperatures. The measured shrinkage (based on LVDT data) for Pellet 4 and the associated temperature profile of the experiment are given in Figure 4-6. The density of Pellet 4 increased during sintering from a green density of 54.0% T.D. to a final density of 58% T.D. This is a relatively small increase, but it should be noted that sintering metals at relatively low temperatures will typically produce low density products. It was noted that densities of 90% T.D. are not normally realized when sintering metal powders below ~90% of the absolute meting temperature [14].

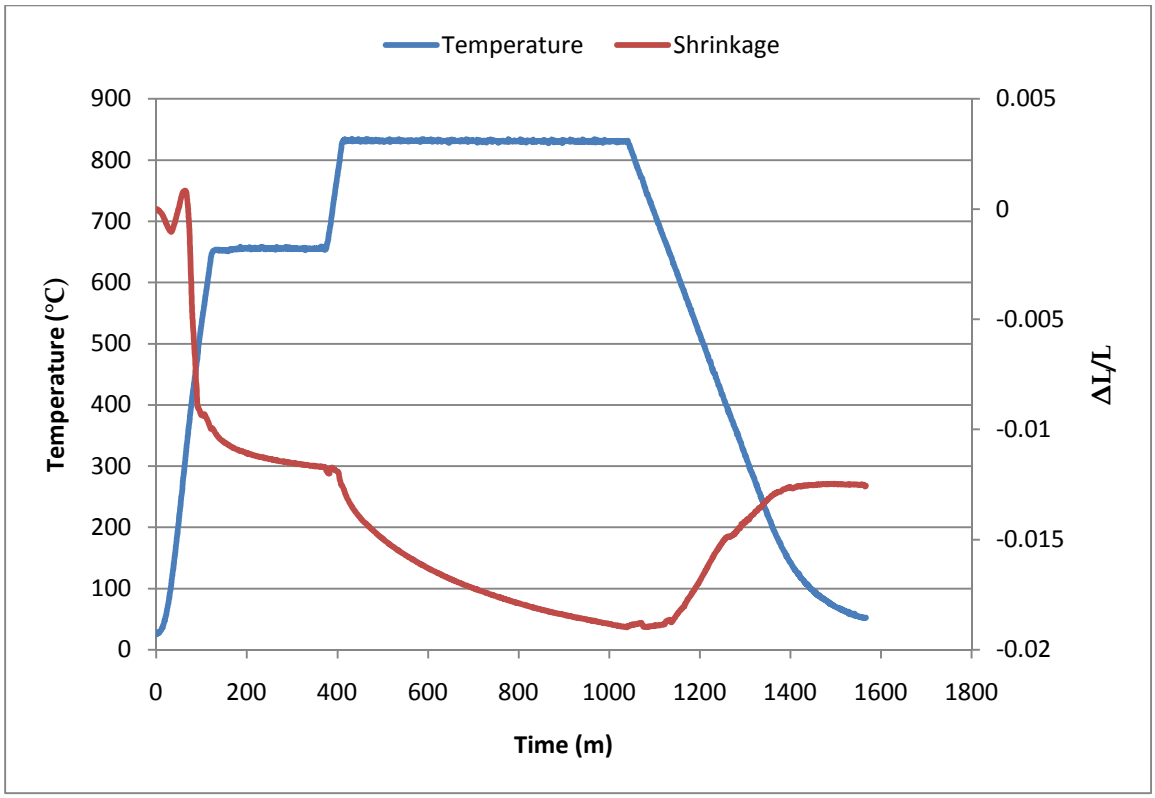

Figure 4-6: Shrinkage and temperature profile for Pellet 4.

Pellet 5 was pressed, using the method described for Pellets 4 and 5, to 47%TD, and was sintered for 6 hours at 643ºC (α-phase), then for 8 hours at 820ºC (γ-phase). A ramp rate of 5ºC/min was used during heating, and a rate of 1ºC/min was used during cooling. An image of Pellet 5 after sintering is given in Figure 4-8. As can be seen in Figure 4-7, a crumbling black layer ~1mm thick formed on the top of Pellet 5 during sintering, and a black powder formed on the sides. This powder was most likely oxidized uranium, formed by leeching oxygen from the ceramic sleeve which held the LVDT rod on top of the pellet.

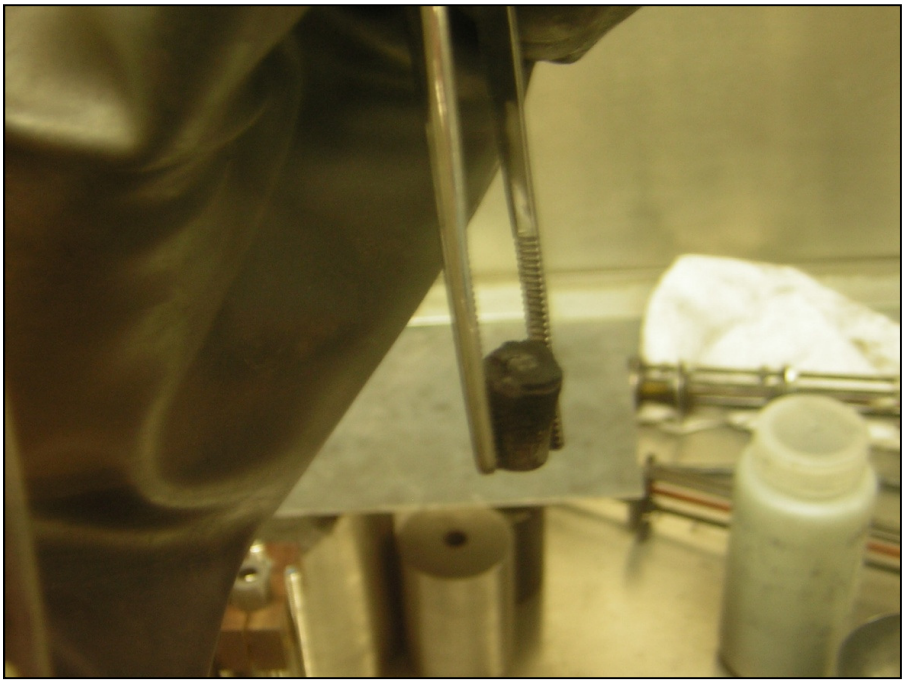

Figure 4-7: Pellet 5 after sintering.

Due to a technical malfunction, LVDT data for a portion of the heating period for Pellet 5 was not recorded; however, the increase in shrinkage before and after heating was consistent with what had previously been observed in Pellets 3 and 4. Sustained shrinkage was observed at both isothermal holding temperatures. The slight expansion observed near the end of the second sintering step was likely due to expansion by oxide formation on the top of the pellet. The measured shrinkage and temperature profile for Pellet 5 are given in Figure 4-8. The density of Pellet 5 increased during sintering from 47%TD to 50%TD.

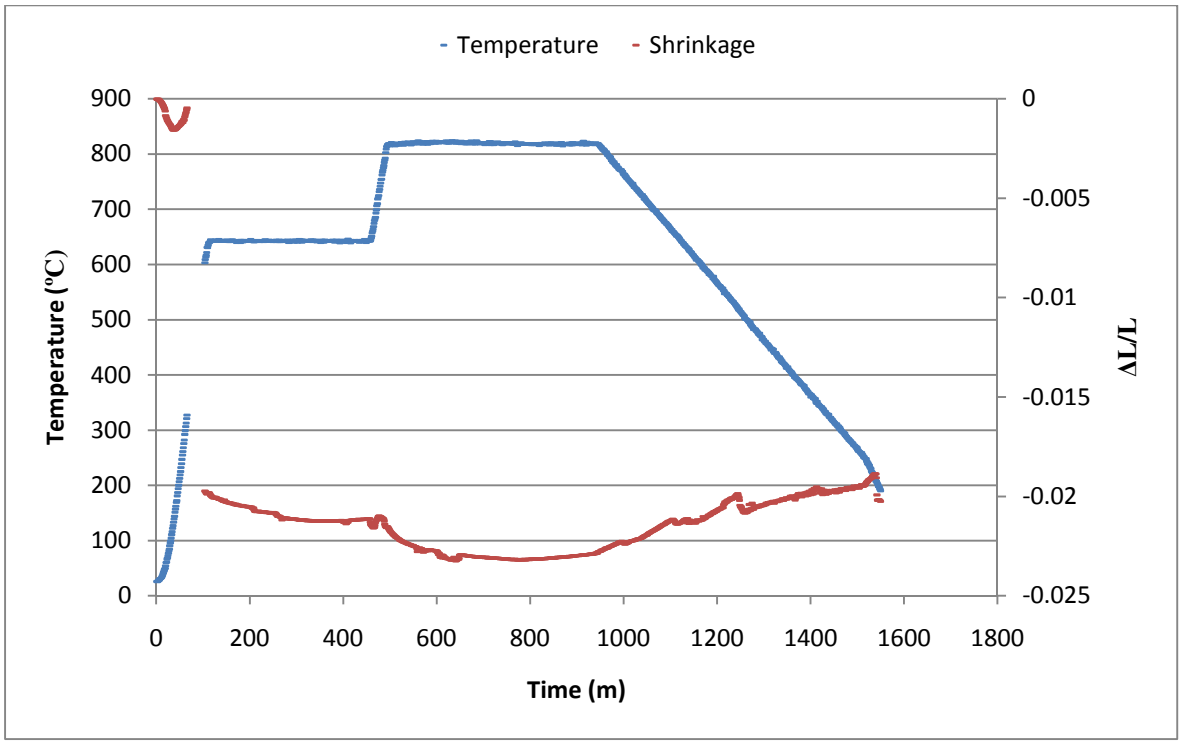

Figure 4-8: Shrinkage and temperature profile for Pellet 5.

Pellet 6 was pressed to 47%TD, and sintered for 8 hours at 634ºC (α-phase), then 8 hours at 809ºC (γ-phase). A ramp rate of 5ºC/min was used during heating, and a rate of 1.5ºC/min was used during cooling. Images of Pellet 6 before and after sintering are given in Figure 4-9 and Figure 4-10 respectively. As can be seen in Figure 4-10, a black oxide layer was once again formed on the top of the pellet. In addition, a portion of this layer was orange tinted, indicated possible contamination with iron.

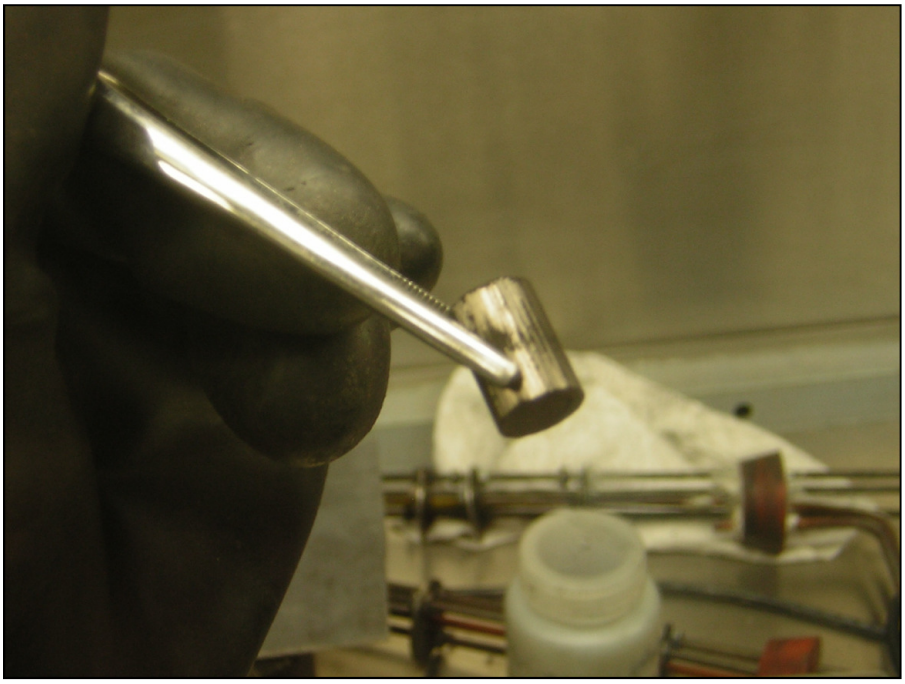

Figure 4-9: Pellet 6 as pressed, before sintering.

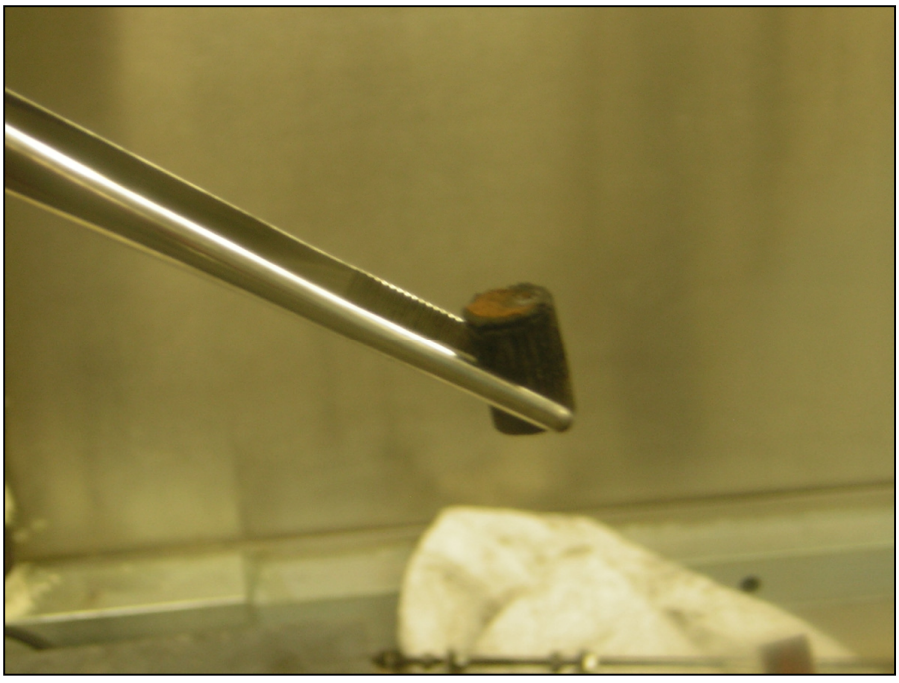

Figure 4-10: Pellet 6 after sintering.

The LVDT data for Pellet 6 showed familiar features from previous pellets. Strong initial shrinkage during heating, gradual shrinkage during isothermal sintering, and eventual expansion due to oxide formation. The measured shrinkage and temperature profile for Pellet 6 are given in Figure 4-11. The density of Pellet 6 increased during sintering from 47%TD to 50%TD.

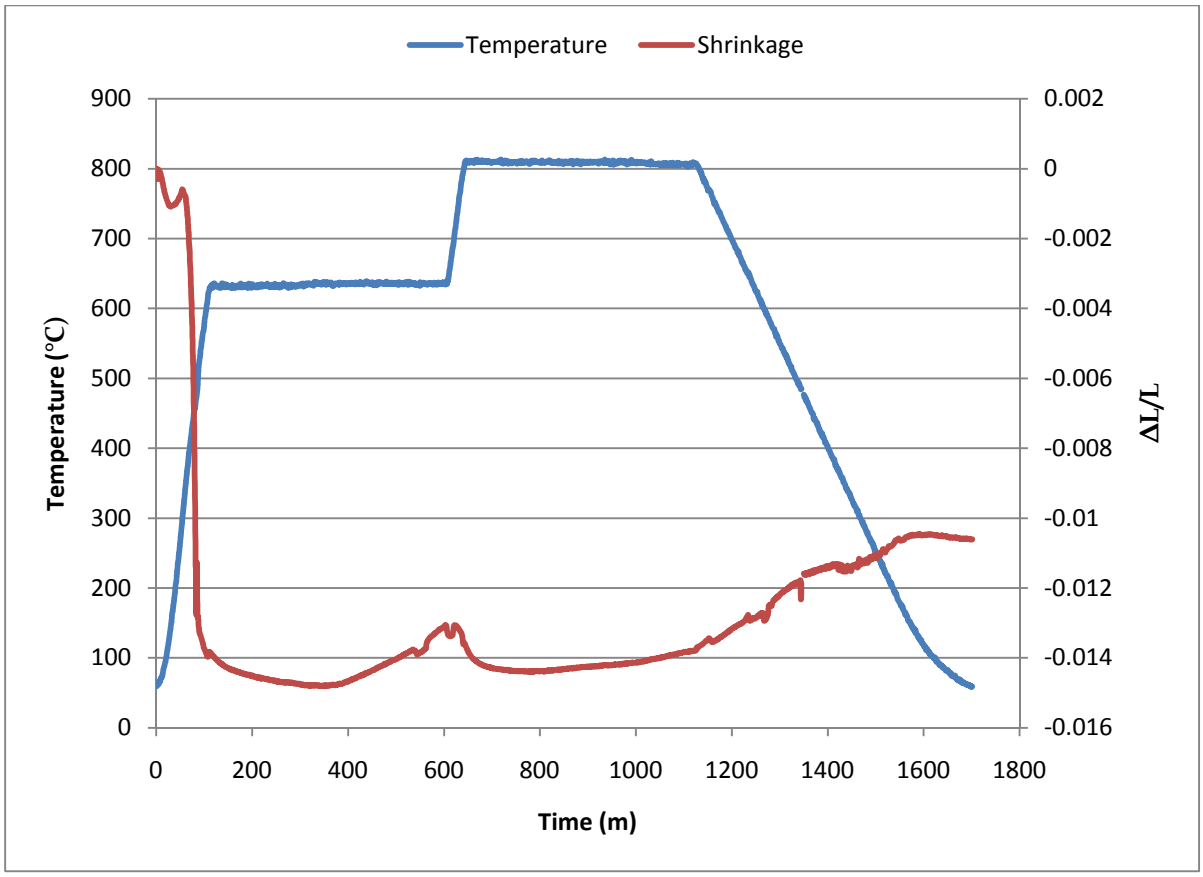

Figure 4-11: Shrinkage and temperature profile for Pellet 6.

Pellet 7 was pressed to 47%TD, and sintered for 9 hours at 659ºC (α-phase), then 8 hours at 834ºC (γ-phase). A ramp rate of 5ºC/min was used during heating, and a rate of 1.5ºC/min was used during cooling. An image of Pellet 7 after sintering are given in Figure 4-12. As can be

seen in Figure 4-12, an oxide coating formed once again on the top and sides of the pellet; however, the thickness of the coating was much less severe.

Figure 4-12: Pellet 7 after sintering.

LVDT data for Pellet 7 showed initial shrinkage during heating and gradual shrinkage during isothermal sintering; however, expansion due to oxide formation was not observed. This was reasonable, given the limited degree of oxide formation seen in Figure 4-12. The measured shrinkage and temperature profile for Pellet 7 are given in Figure 4-13. The density of Pellet 7 increased during sintering from 47%TD to 51%TD.

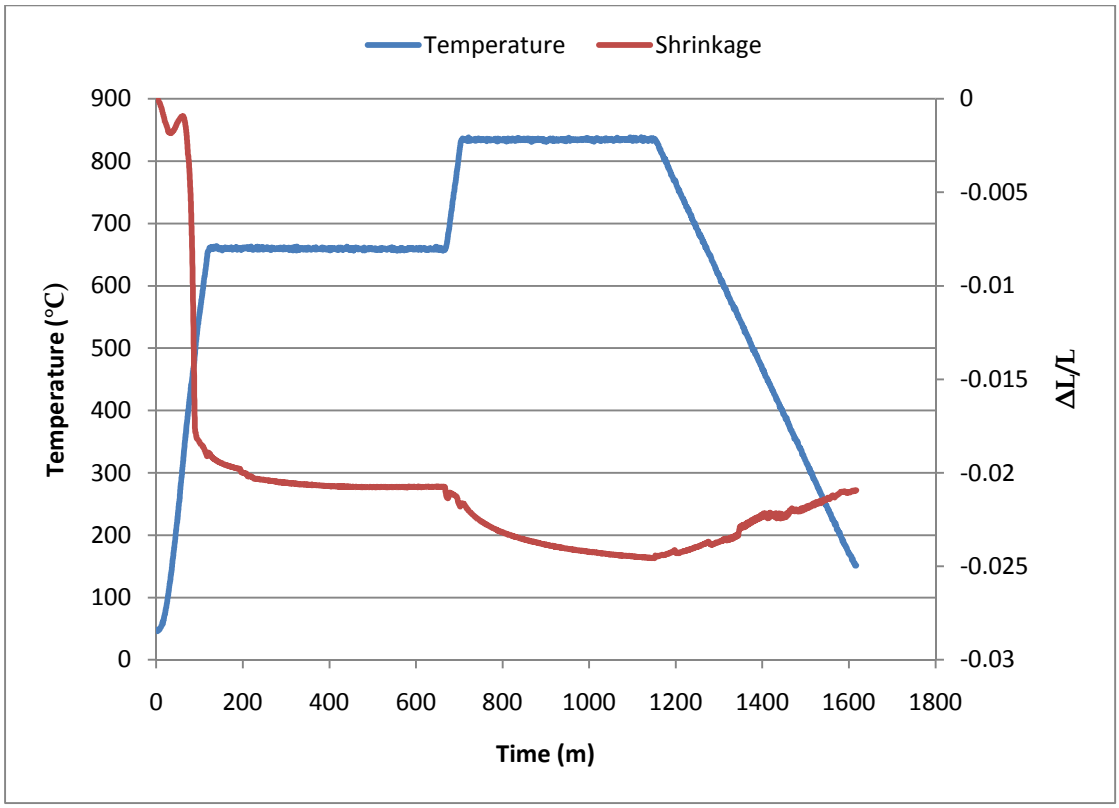

Figure 4-13: Shrinkage and temperature profile for Pellet 7.

Pellet 8 was pressed to 48%TD, and sintered for 8 hours at 651ºC (α-phase), then 7 hours at 826ºC (γ-phase). A ramp rate of 5ºC/min was used during heating, and a rate of 1.5ºC/min was used during cooling. An image of Pellet 8 after sintering is given in Figure 4-14. Similar to Pellet 7, Pellet 8 formed a light oxide powder coating on the top and sides of the pellet during sintering, as can be seen in Figure 4-14.

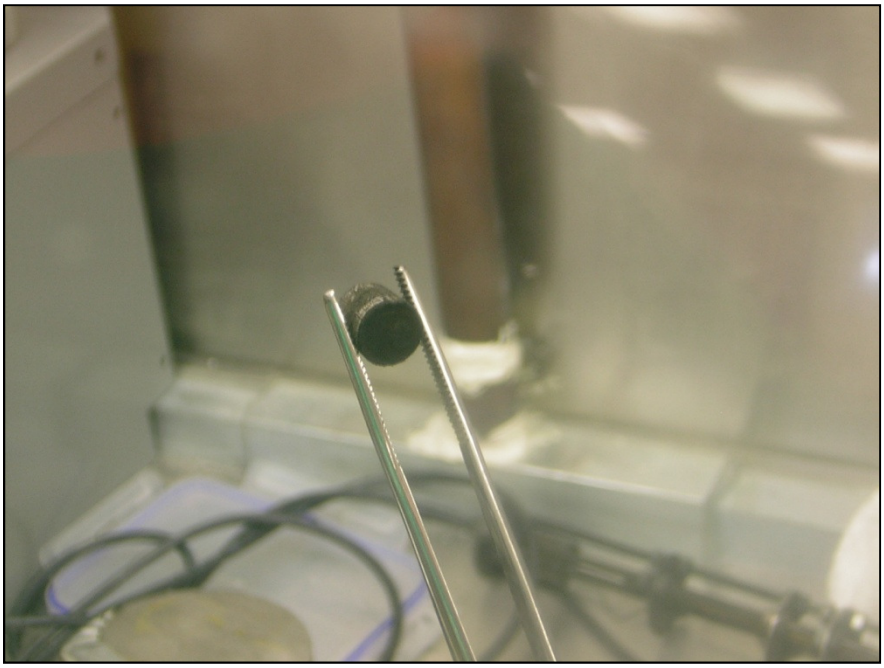

Figure 4-14: Pellet 8 after sintering.

LVDT data for Pellet 8 showed initial shrinkage during heating and gradual shrinkage during isothermal sintering. The measured shrinkage and temperature profile for Pellet 8 are given in Figure 4-15. The density of Pellet 8 increased during sintering from 48%TD to 52%TD.

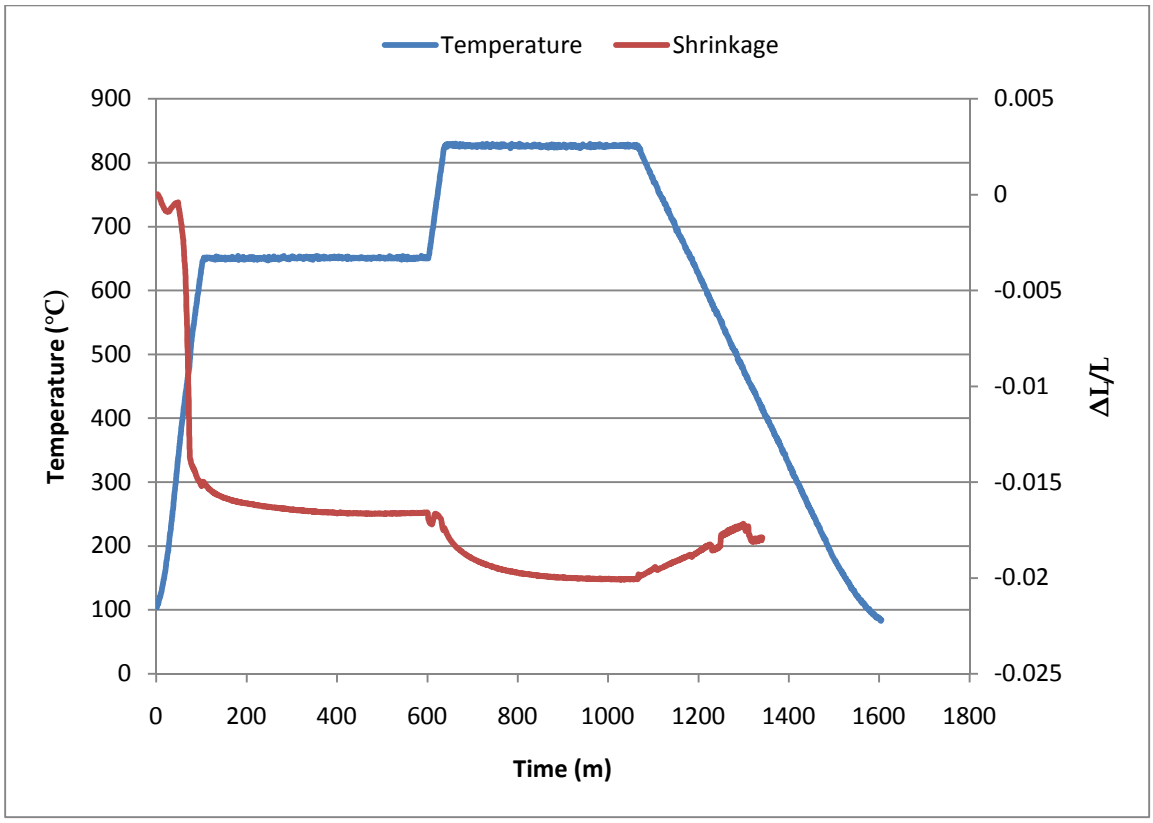

Figure 4-15: Shrinkage and temperature profile for Pellet 8.

The α-phase isothermal region of each pellet which demonstrated sintering was analyzed using Equation 3-2 to determine the value of *n*, as described in the models given in Section 2.1.3. The resulting plot is shown in Figure 4-16. Linear trendlines were fitted to the results for each pellet, producing the effective value of *n* for each pellet. These values are reported in Table 4-2. The data used to determine *n* contains some natural variations, observable as slight deviations from linearity in Figure 4-16; however, these minor variations did not appear to significantly affect the results.

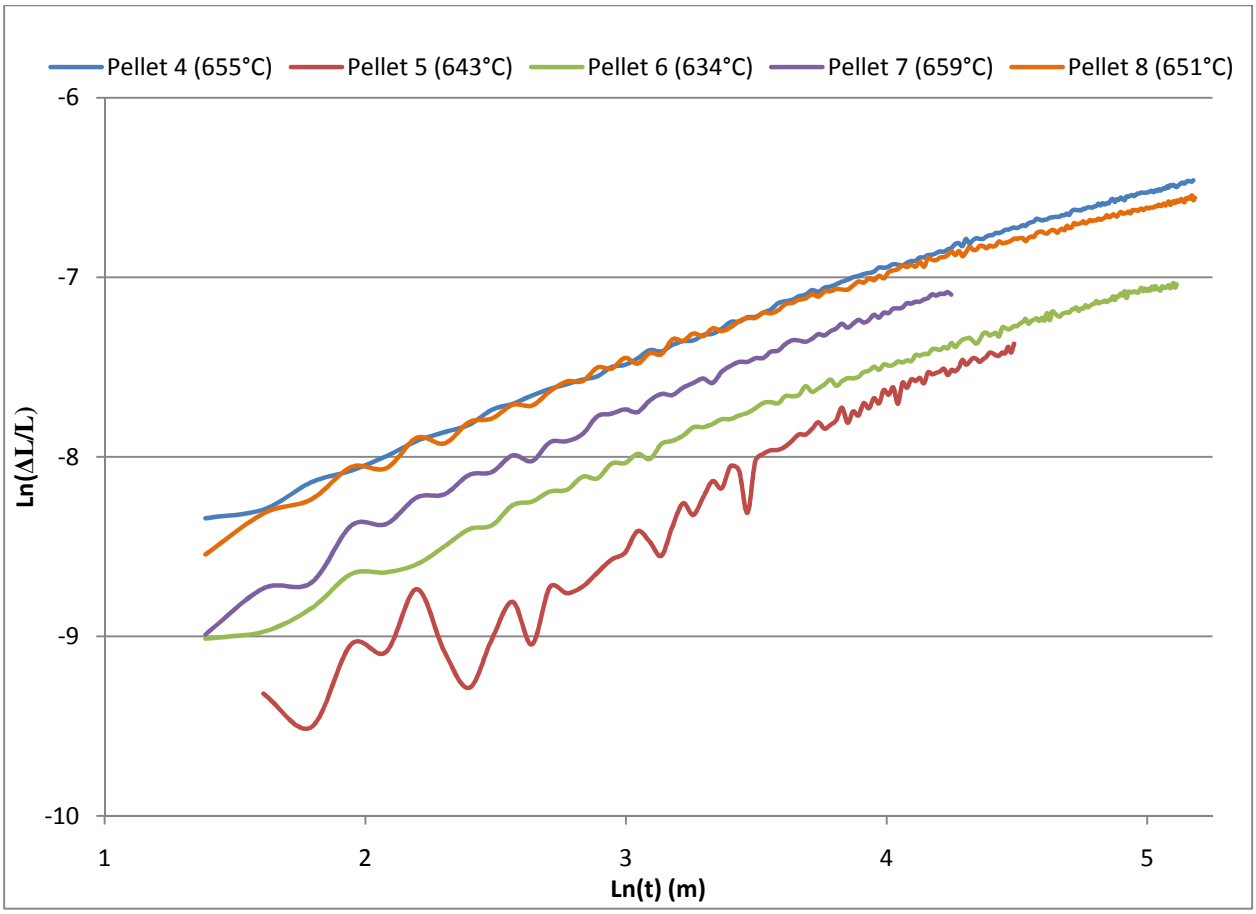

Figure 4-16: Log-log plot of shrinkage vs. time for determination of DU sintering constants.

Table 4-2: Calculated values of *n* for isothermal α-phase sintering of pure DU.

	Contents	α-Phase Temperature	Calculated *n*	R^2
Pellet 4	DU	655°C	4.11	0.9933
Pellet 5	DU	643°C	2.60	0.9693
Pellet 6	DU	634°C	3.93	0.9860
Pellet 7	DU	659°C	3.26	0.9870
Pellet 8	DU	651°C	4.36	0.9812

The activation energy, *Q*, for α-phase sintering of uranium was determined by using Equation 3-4 to construct an Arrhenius plot of the shrinkage after three hours for Pellet 4, Pellet 6, Pellet

7, and Pellet 8. Pellet 5 was excluded as an outlier, for reasons discussed later in Section 5.2.1. The resulting Arrhenius plot is given in Figure 4-17. Based on this plot and the previously determined value of *n*, the activation energy for α-phase uranium sintering was 340 +/-41 kJ/mol.

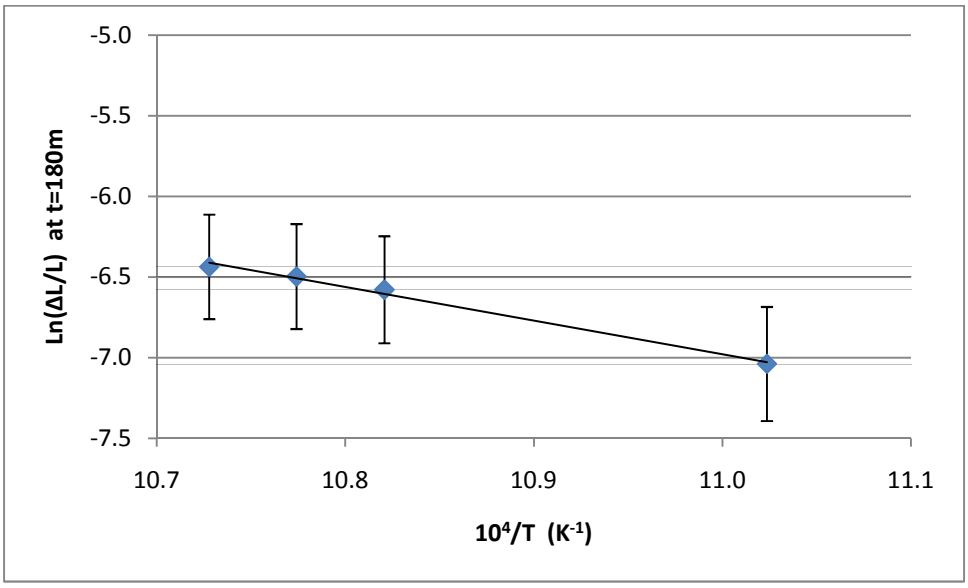

Figure 4-17: Arrhenius plot for α-phase sintering of uranium.

4.2.2 BSE Imaging of Sintered Uranium

Backscatter Electron (BSE) imaging was performed on a cross section of each of the successfully sintered uranium pellets. The cross section of each pellet demonstrated a pronounced dog-bone shaped region of higher sintered density in the center of the pellet, and an outer region of lower density. This effect can clearly be seen in the optical image of Pellet 4, shown in Figure 4-18.

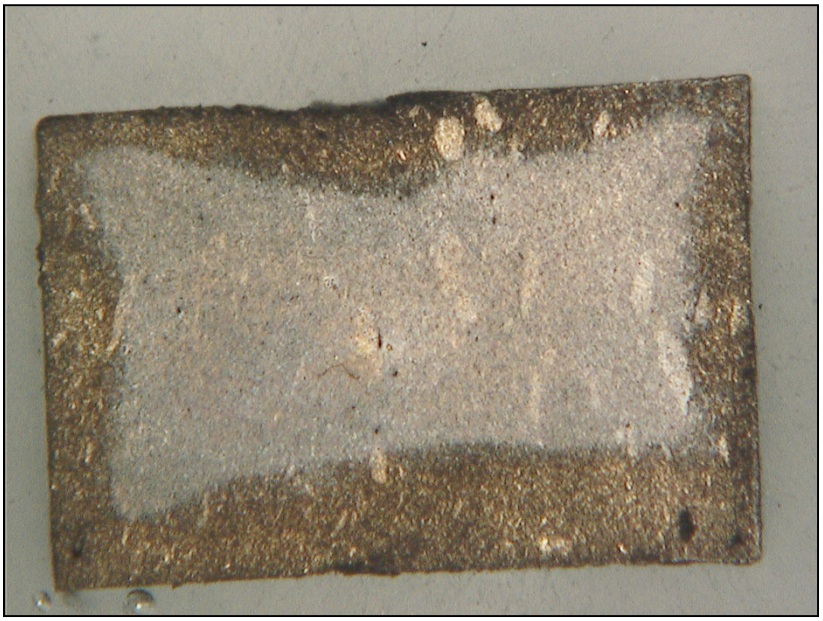

Figure 4-18: Polished cross section of Pellet 4 at 25x magnification demonstrating inner and outer regions.

The difference in microstructure between the inner and outer sintered regions is shown in Figure 4-19. In this BSE image of Pellet 4, the upper section shows the relatively high porosity region near the edge of the pellet, while the lower section shows the relatively low porosity region near the center of the pellet. Even in the more porous section of the pellet, the size of the pores was fairly uniform, with very few large pores. This result was typical for each of the sintered pellets. One of the few larger pores observed in the samples is shown in Figure 4-20.

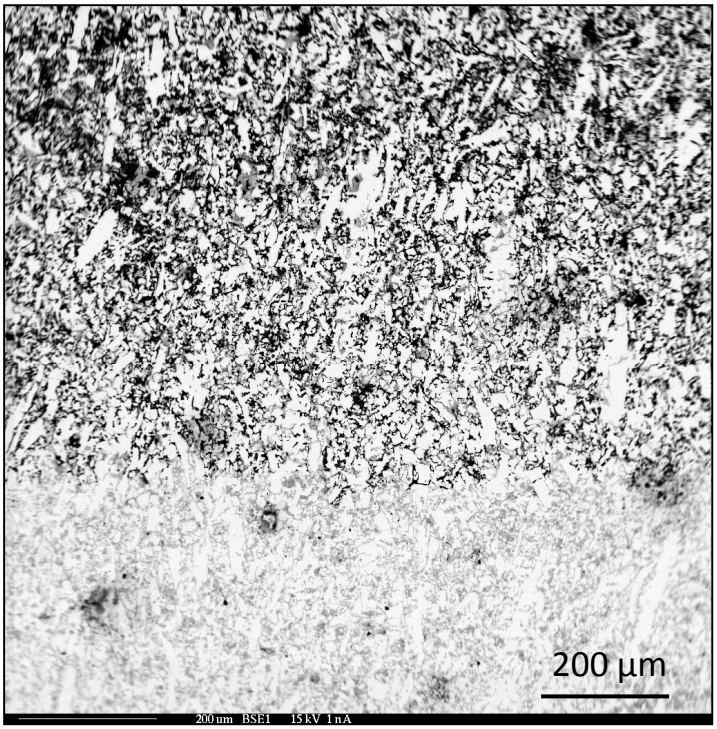

Figure 4-19: BSE image of boundary between low and high porosity regions of Pellet 4.

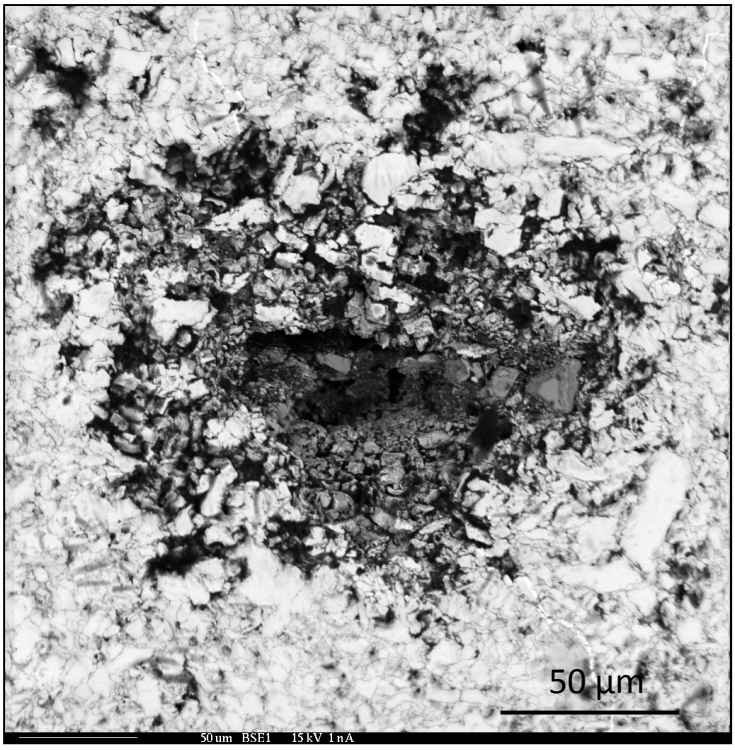

Figure 4-20: BSE image of rare, larger pore in Pellet 8.

For the most part, the sintered pellets did not show signs of cracking due to delamination during cooling. There were only two cases in which cracks greater than several microns long were formed, and in each case these cracks occurred near the edge of the pellets in the high porosity region. Images of these cracks are shown in Figures 4-21, 4-22, and 4-23.

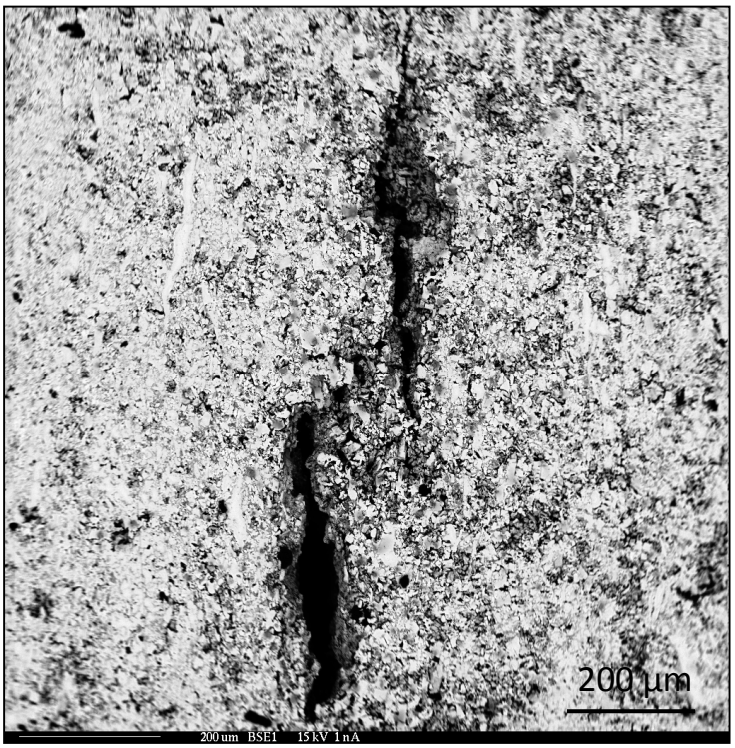

Figure 4-21: BSE image of cracking in Pellet 6.

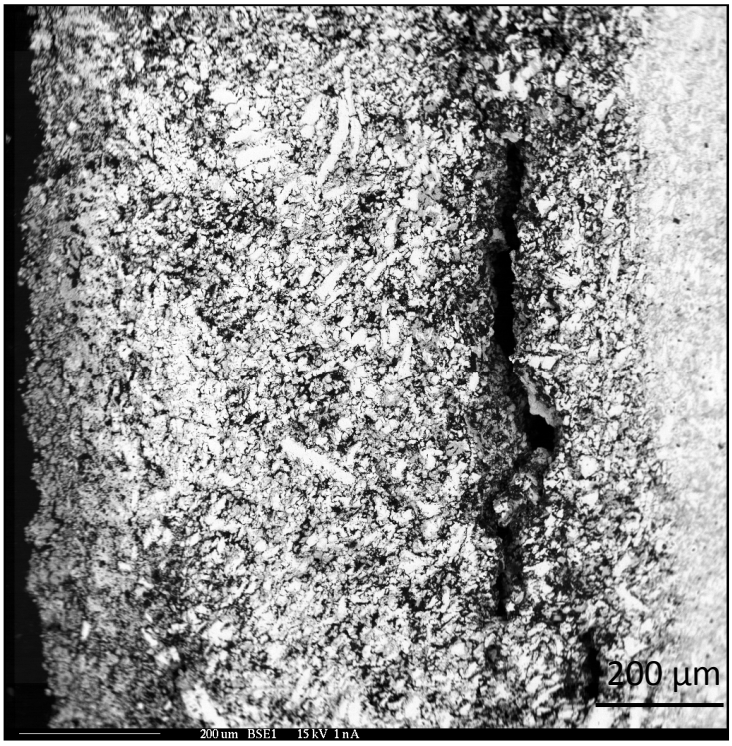

Figure 4-22: BSE image of cracking in Pellet 7.

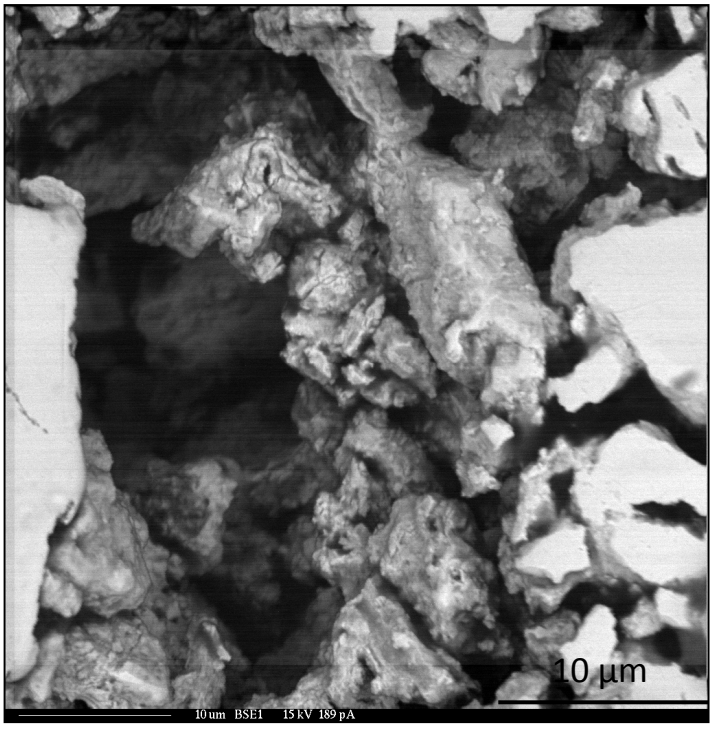

Figure 4-23: BSE image within large crack in Pellet 6.

Although large cracks showing delamination were rare, series of small cracks potentially demonstrating delamination were observed in some pellets. The length of these cracks were typically on the order of 10 microns. An examples of these micro-cracks is shown in Figure 4-24.

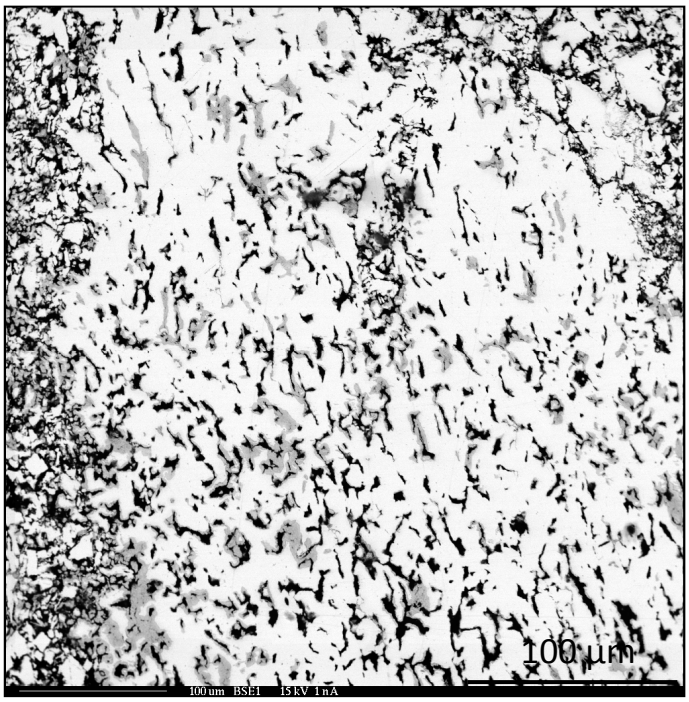

Figure 4-24: BSE image of small cracks in Pellet 5.

A series of images of each pellet were analyzed to determine the porosity of each pellet within the low porosity inner region and the high porosity outer region. The results of this analysis are given in Table 4-3.

Table 4-3: Porosity of sintered uranium pellets as determined from SEM images.

	Porosity of Outer Region	Porosity of Inner Region
Pellet 4	32.3%	11.5%
Pellet 5	36.2%	13.2%
Pellet 6	40.0%	9.7%
Pellet 7	30.9%	3.2%
Pellet 8	23.0%	1.1%

4.2.3 Isothermal Sintering of DU-10Zr

The second set of experiments performed sintered DU-10Zr pellets isothermally at several temperatures in the α and γ phases. A total of three DU-10Zr pellets were fabricated, and each pellet was successfully sintered. A summary of the conditions and properties of each pellet is given in Table 4-4. Based on experiences with fabrication of uranium pellets described in Section 4.2.1, each U-10Zr pellet was pressed with a force of 44.5 kN (10,000 lbf) for 15 seconds.

Table 4-4: Summary of isothermally sintered DU-10Zr pellets.

Pellet #	Powder Source	Contents	α-Temperature	γ-Temperature	Green Density	Sintered Density
9	H/dH Run 4	DU-10Zr	635 °C	817 °C	51.27%	55.74%
10	H/dH Run 4	DU-10Zr	642 °C	819 °C	50.67%	55.80%
11	H/dH Run 4	DU-10Zr	652 °C	829 °C	51.28%	56.47%

Pellet 9 was pressed to 51%TD, and sintered for 7 hours at 635ºC (α-phase), then 6 hours at 817ºC (γ-phase). A ramp rate of 5ºC/min was used during heating, and a rate of 1.5ºC/min was used during cooling. Images of Pellet 9 before and after sintering are given in Figure 4-25 and

Figure 4-26 respectively. As can be seen in Figure 4-26, some black powder formation still occurred on the top of the pellet during sintering; however, the severity of the phenomena continued to decrease relative to previous pellets.

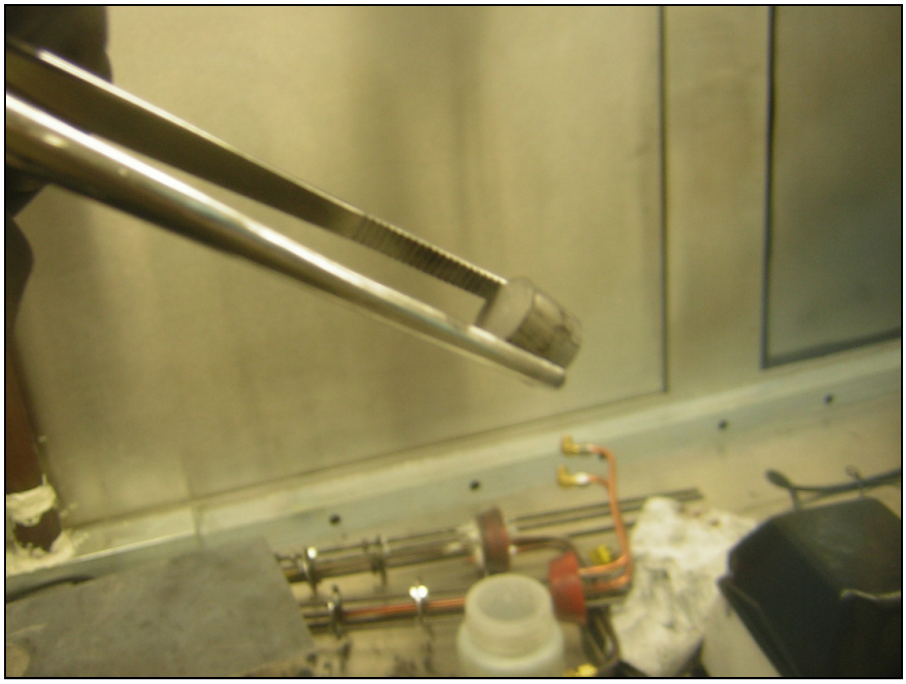

Figure 4-25: Pellet 9 as pressed, before sintering.

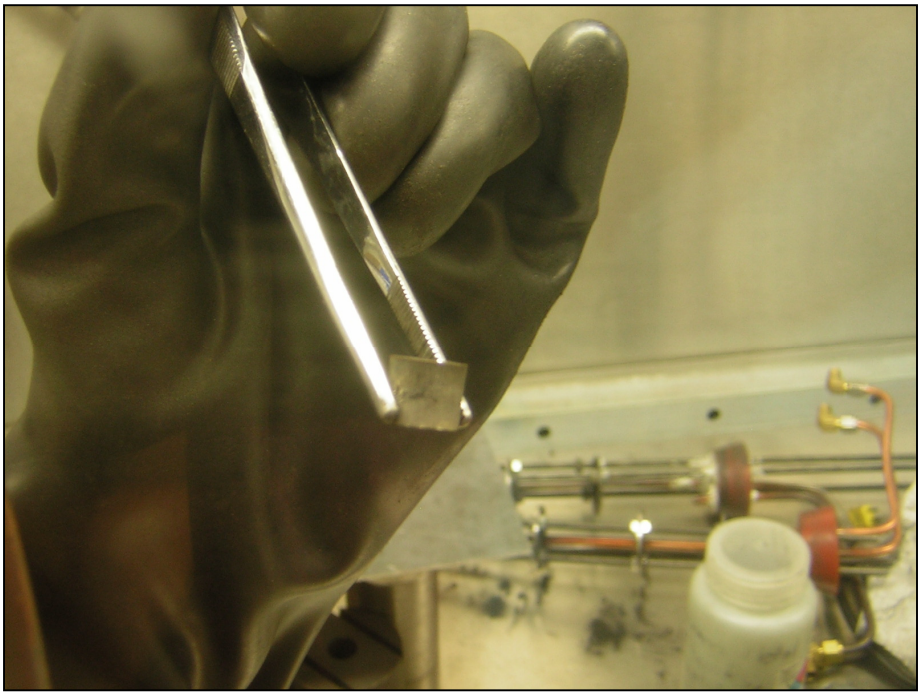

Figure 4-26: Pellet 9 after sintering.

The LVDT data for Pellet 9 showed a couple of distinct differences from the DU samples in the previous section. First, a smaller degree of shrinkage was observed during heating and second, the shrinkage in both the α and γ phase were much more pronounced than for pure uranium pellets. Further, there was a slight deflection in the shrinkage vs. time curve for the γ-phase sintering portion of the experiment. The measured shrinkage and temperature profile for Pellet 9 are given in Figure 4-27. The density of Pellet 9 increased during sintering from 51%TD to 56%TD.

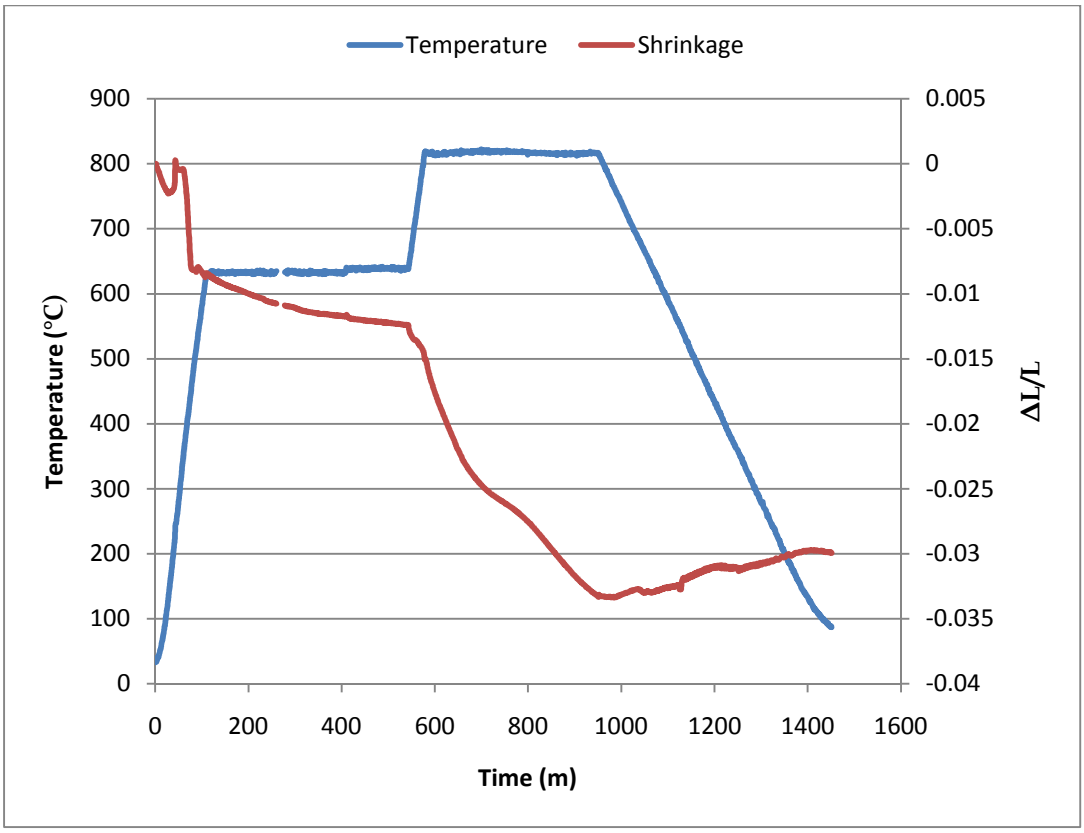

Figure 4-27: Shrinkage and temperature profile for Pellet 9.

Pellet 10 was pressed to 51%TD, and sintered for 7 hours at 642ºC (α-phase), then 7 hours at 819ºC (γ-phase). A ramp rate of 5ºC/min was used during heating, and a rate of 1.5ºC/min was used during cooling. Images of Pellet 10 before and after sintering are given in Figure 4-28 and Figure 4-29 respectively. The appearance of Pellet 10 after sintering was very similar to Pellet 9; a light formation of black powder was formed on the top of pellet.

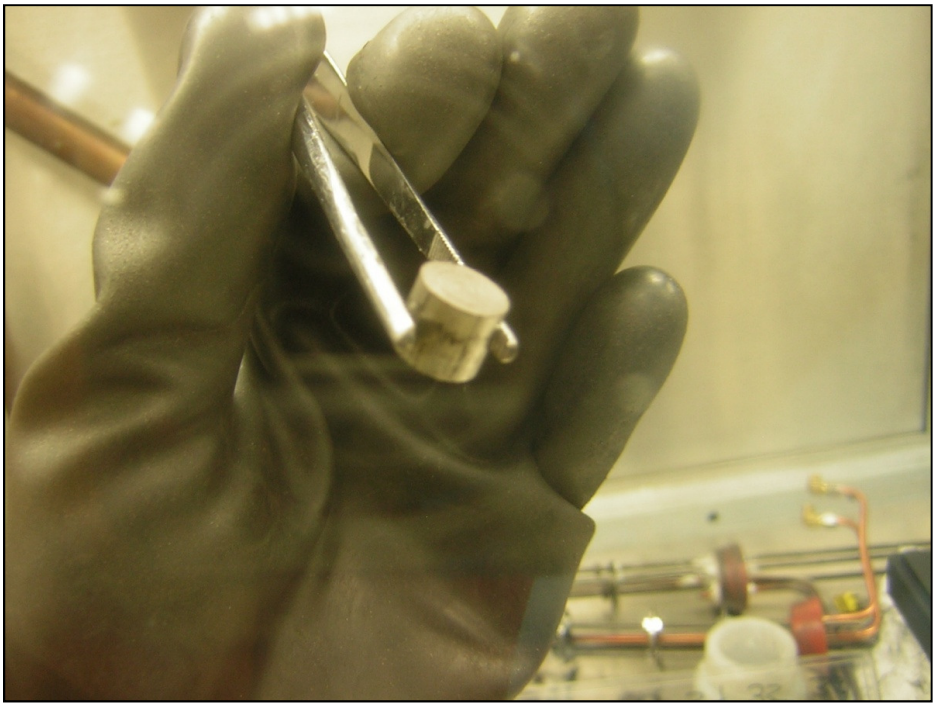

Figure 4-28: Pellet 10 as pressed, before sintering.

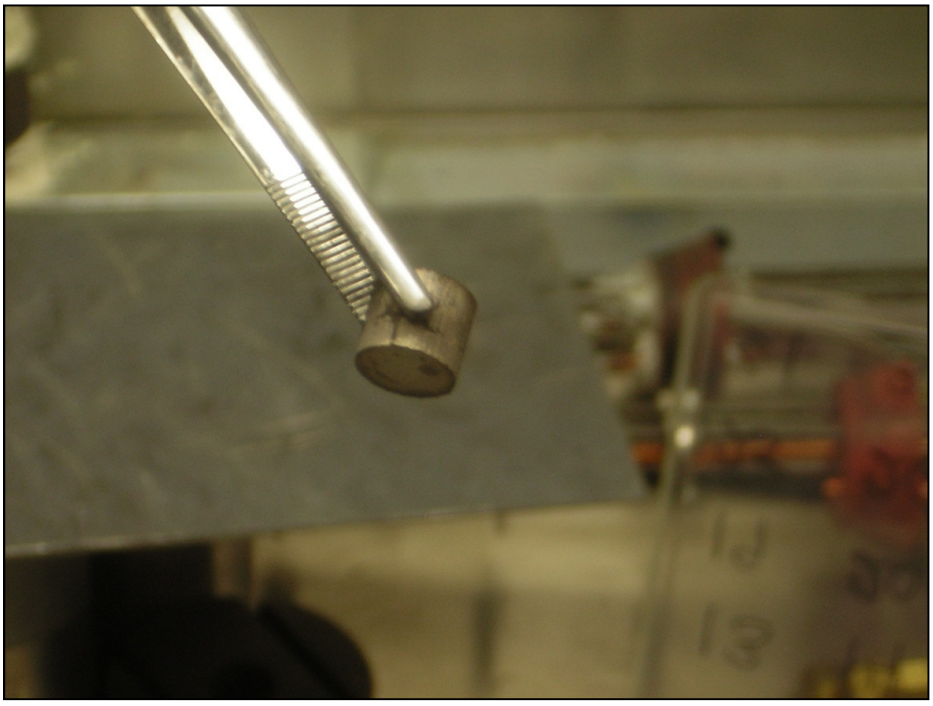

Figure 4-29: Pellet 10 after sintering.

The LVDT data for Pellet 10 was very similar to Pellet 9, demonstrating reduced shrinkage during heating and enhanced shrinkage during isothermal sintering relative to pure uranium pellets. In addition, the hump in shrinkage was once again observed during isothermal γ-phase sintering. The measured shrinkage and temperature profile for Pellet 10 are given in Figure 4-30. The density of Pellet 10 increased during sintering from 51%TD to 56%TD.

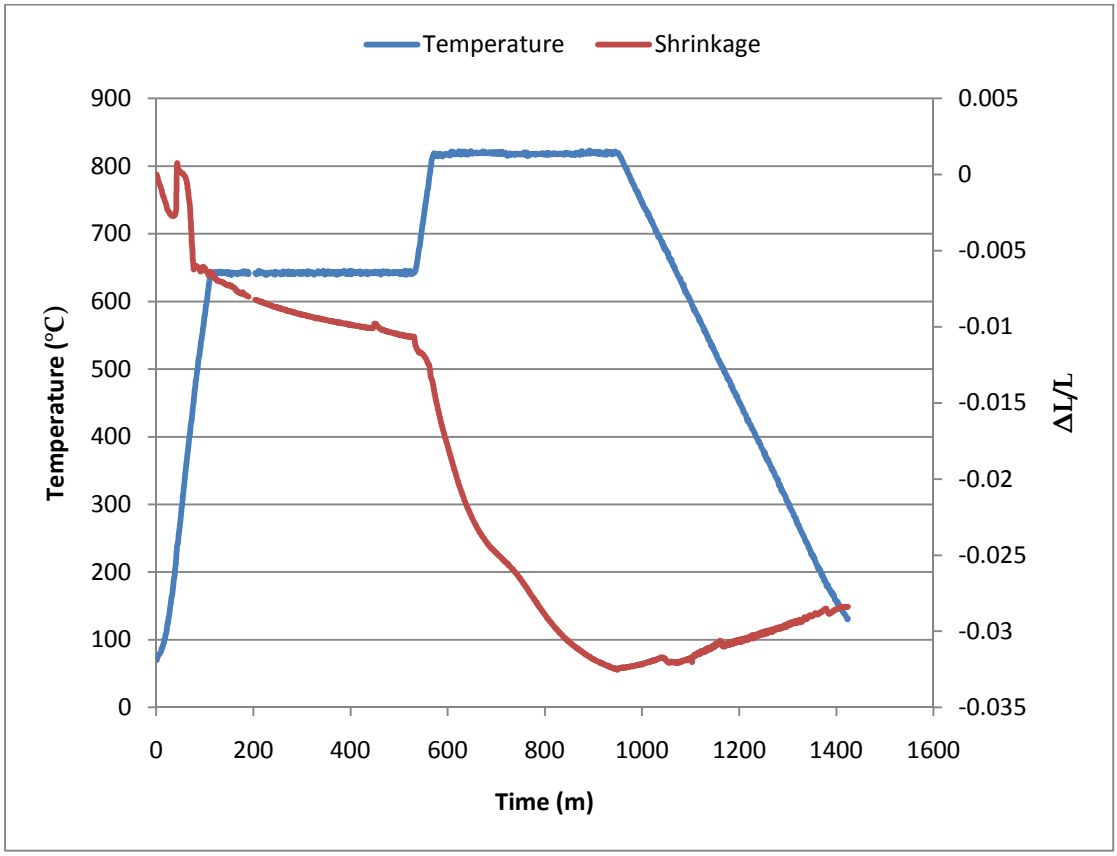

Figure 4-30: Shrinkage and temperature profile for Pellet 10.

Pellet 11 was pressed to 51%TD, and sintered for 7 hours at 652ºC, then 3 hours at 829ºC. The relatively short sintering time in the gamma phase was due to operator error, which also resulted in uncontrolled cooling following sintering. In spite of this deviation, the sintering

behavior of Pellet 11 was still very similar to that of Pellet 9 and Pellet 10. Images of Pellet 11 before and after sintering are given in Figure 4-31 and Figure 4-32 respectively.

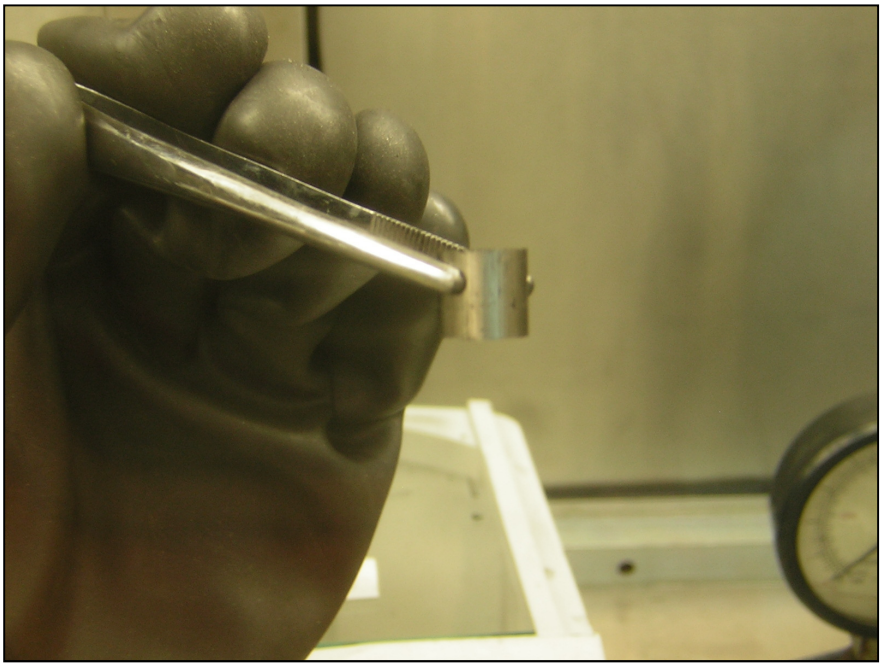

Figure 4-31: Pellet 11 as pressed, before sintering.

Figure 4-32: Pellet 11 after sintering.

The LVDT data for Pellet 11 showed some initial shrinkage during heating and steady shrinkage during isothermal sintering. The hump in shrinkage previously observed in γ-phase sintering DU-10Zr pellets was once more evident, although it was terminated prematurely by the shortened γ-phase sintering time. The measured shrinkage and temperature profile for Pellet 11 are given in Figure 4-33. The density of Pellet 11 increased during sintering from 51%TD to 56%TD.

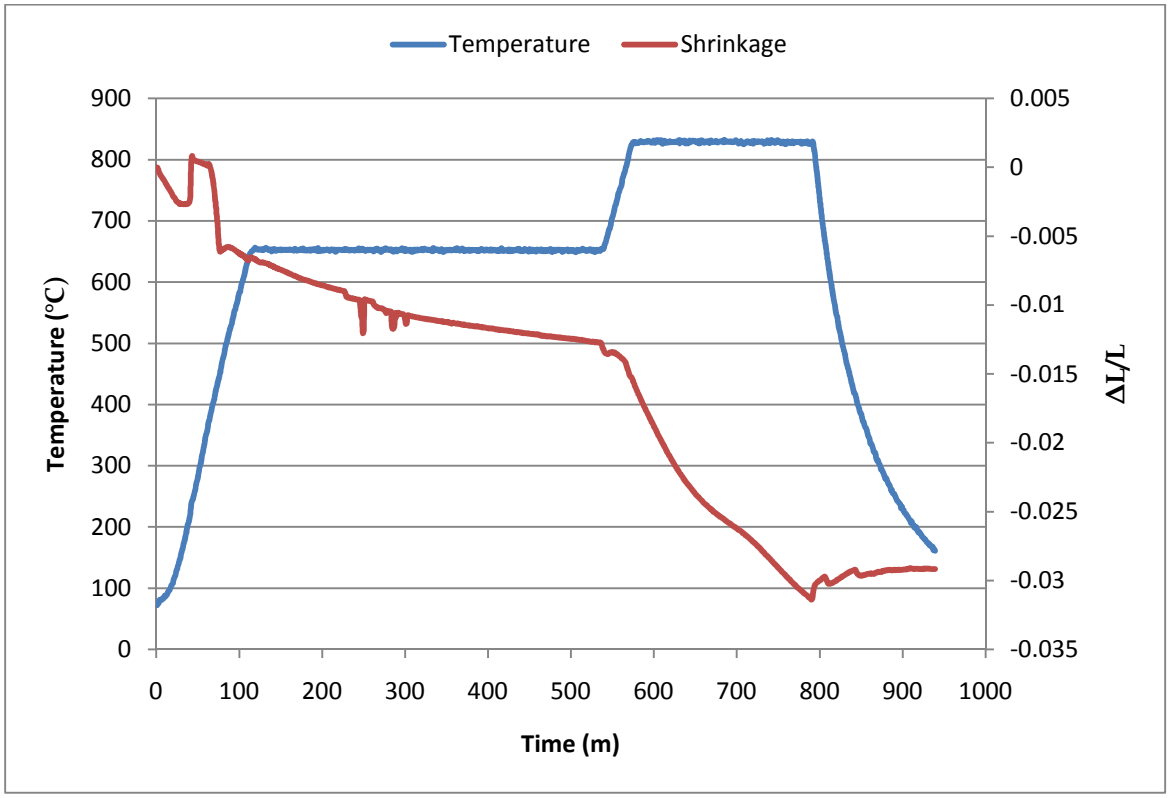

Figure 4-33: Shrinkage and temperature profile for Pellet 11.

As was done for isothermally sintered pellets of pure DU, the α-phase sintering of U-10Zr pellets was analyzed to determine the value of *n*. The plot used in these calculations is shown in Figure 4-33. The resulting values of *n* for each U-10Zr pellet are given in Table 4-5. As was observed previously in Figure 4-16, some oscillation in occurs in Figure 4-34, particularly in the

early stages of sintering. The appearance of these oscillations are exaggerated in the early stages due to the logarithmic nature of the graph. The calculated values of *n* for DU-10Zr were significantly lower than those calculated for DU, indicating a more rapid rate of sintering.

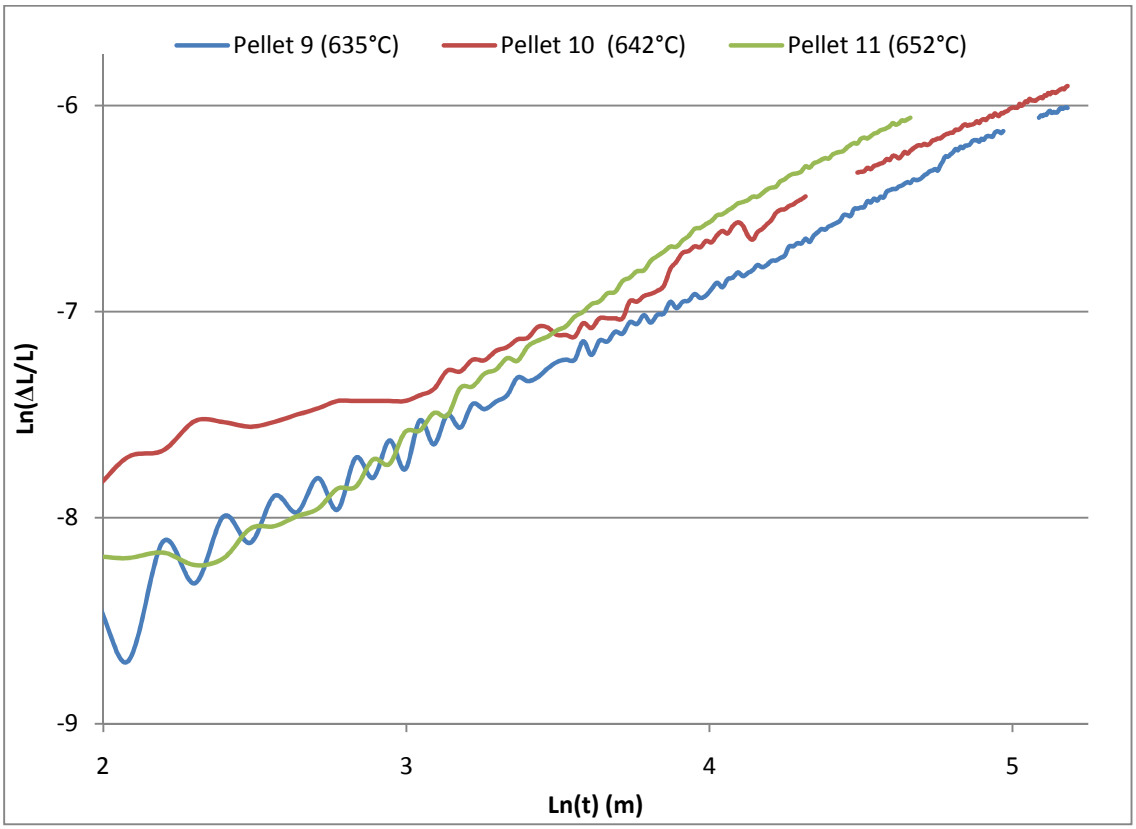

Figure 4-34: Log-log plot of shrinkage vs. time for determination of DU-10Zr sintering constants.

Table 4-5: Calculated values of *n* for isothermal α-phase sintering of DU-10Zr.

	Contents	α-Phase Temperature	Calculated *n*	R^2
Pellet 9	DU-10Zr	635°C	2.55	0.9871
Pellet 10	DU-10Zr	642°C	2.29	0.9855
Pellet 11	DU-10Zr	652°C	3.11	0.9876

The activation energy, *Q*, for α-phase sintering of U-10Zr was determined based on an Arrhenius plot of the shrinkage after three hours for Pellet 9, Pellet 10, and Pellet 11. The resulting Arrhenius plot is given in Figure 4-34. Based on this plot and the previously determined value of *n*, the activation energy for α-phase U-10Zr sintering was 272 +/-91 kJ/mol

.

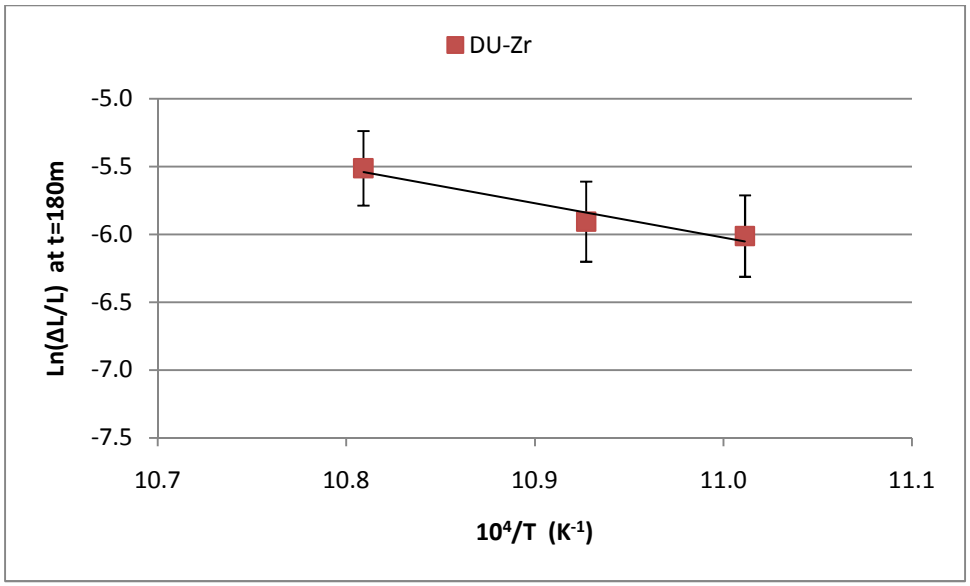

Figure 4-35: Arrhenius plot for α-phase sintering of DU-10Zr.

4.2.4 BSE Imaging of Sintered DU-10Zr

As was observed in sintered uranium pellets, pellets of DU-10Zr included a dog-bone shaped inner region of lower porosity and an outer region of higher porosity. The difference between these two regions is shown in Figures 4-36 and 4-37. In these images, white regions represent uranium, gray regions represent zirconium, and black regions represent pores. In addition to showing the pore microstructure, Figures 4-36 and 4-37 also show the distribution of zirconium in the DU-10Zr pellets. Although large particles of zirconium remain, they are distributed

throughout the material, and a portion of the zirconium has diffused into the surrounding uranium.

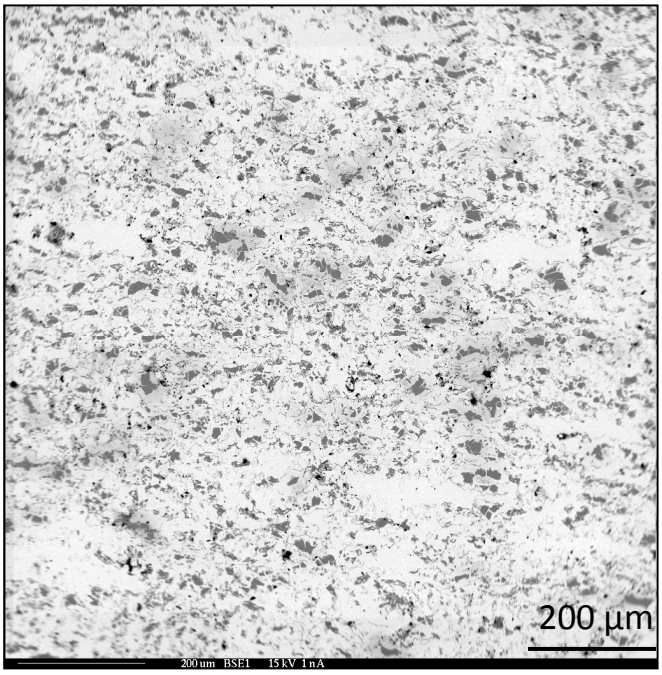

Figure 4-36: BSE image of inner, low porosity region of Pellet 9.

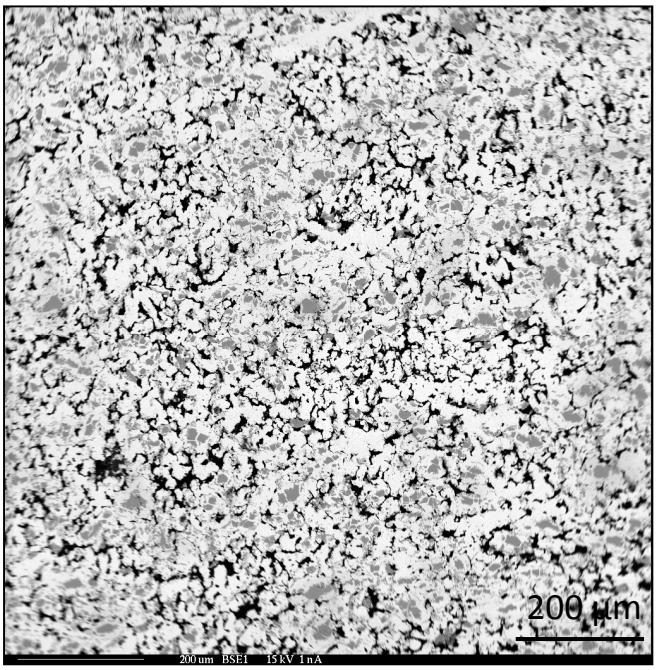

Figure 4-37: BSE image of outer, high porosity region of Pellet 10.

Images taken at higher magnifications of the DU-10Zr pellets showed the formation of mixed uranium-zirconium microstructure in regions surrounding zirconium particles, as shown in Figures 4-38 and 4-39. In addition, small amounts of zirconium were observed within the uranium, even in areas further away from zirconium particles. Quantitative analysis by Wavelength Dispersive Spectrometer (WDS) provided average elemental compositions in each region of the DU-10Zr pellets as described in Table 4-6.

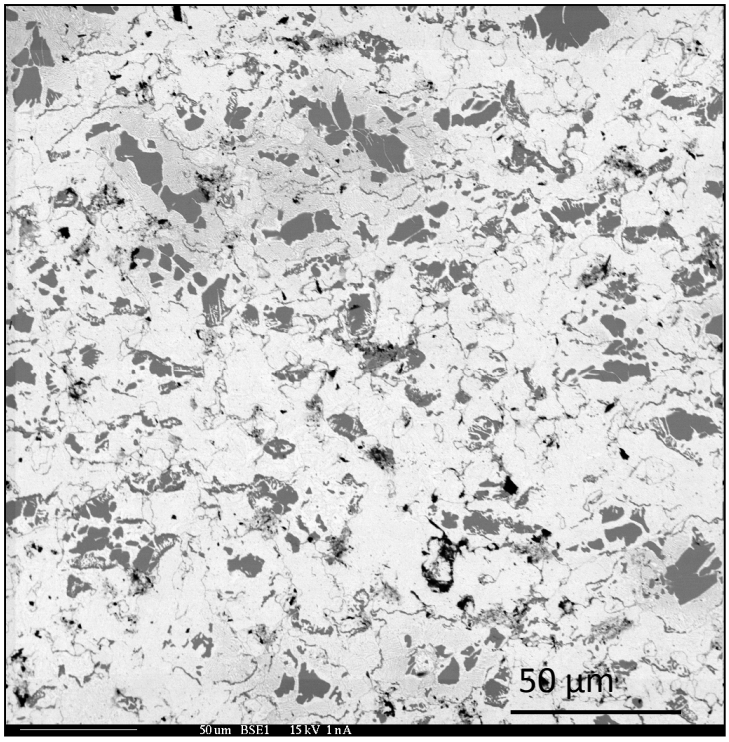

Figure 4-38: BSE image of Pellet 9 showing U-Zr microstructure.

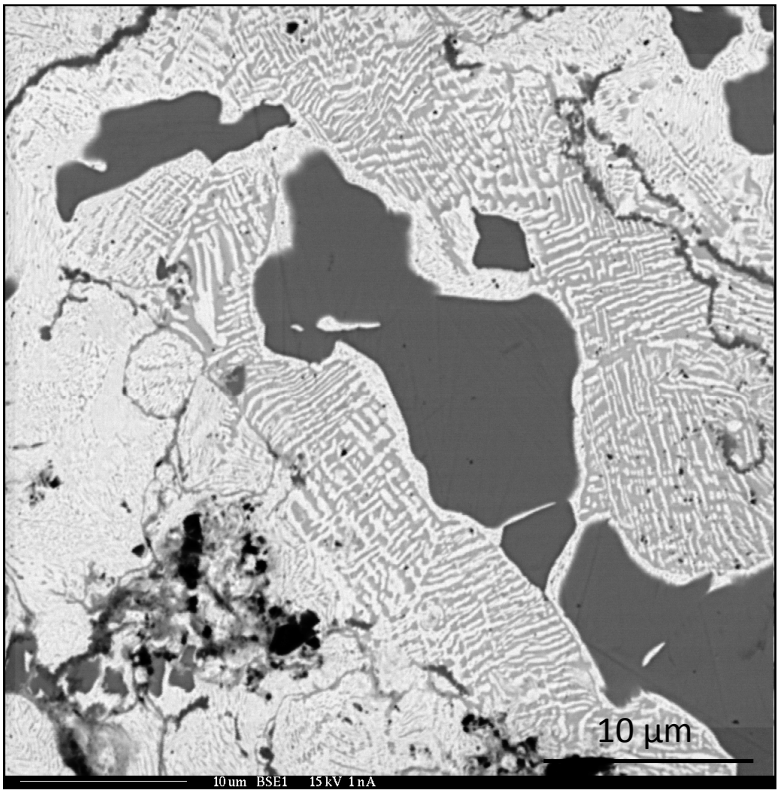

Figure 4-39: BSE image of Pellet 9 showing further U-Zr microstructure.

Table 4-6: Average elemental composition of various regions in DU-10Zr pellets.

	Zr Atom%	U Atom%
Zirconium Particles	99.998	0.002
Lamellar Structure	41.251	58.749
Bulk Uranium	13.628	86.372

As was done previously with uranium pellets, a series of images of each DU-10Zr pellet were analyzed to determine the porosity of each pellet within the low porosity inner region and the high porosity outer region. The results of this analysis are given in Table 4-7.

Table 4-7: Porosity of sintered DU-10Zr pellets as determined from SEM images.

	Porosity of Outer Region	Porosity of Inner Region
Pellet 9	12.0%	1.0%
Pellet 10	14.2%	1.5%
Pellet 11	8.7%	5.8%

4.2.5 Sintering of DU-5Zr

After completion of isothermal sintering studies on DU and DU-10Zr pellets, a final series of sintering experiments were performed using DU-5Zr pellets. These experiments focused on complementing the results previously obtained and filling in any gaps in knowledge. The two basic sintering experiments performed with DU-5Zr were extended alpha-phase sintering and sintering with cyclical alpha/beta phase transitions.

Imaging of previously sintered pellets indicated the consistent presence of inner regions with low porosity and outer regions with higher porosity. In an effort to reduce this effect, Pellet 14 was compacted with increased force and sintered in the alpha phase for a significantly longer period. The compaction force was doubled, to 89 kN (20,000 lbf). This resulted in a green density of 48.8%TD.

Pellet 14 was sintered in the alpha phase for 48 hours at a temperature of 650°C. Shrinkage data for this run is unavailable, due to a technical malfunction; however, the sintered density was measured to be 52.5%.

BSE images of a cross-section of Pellet 14, shown in Figures 4-40 and 4-41, show that it sintered to a very low porosity solid. Image analysis calculated 0.5% porosity, which was consistent across the entire cross-section. Quantitative analysis of Pellet 14 showed three primary regions. First, areas of pure zirconium were spread throughout the pellet. Second,

bands of UZr_2 on the order of 10 microns thick surrounded each of the pure zirconium areas. Finally, the remainder of the material consisted of uranium containing small amounts of zirconium. The grain boundaries in this region were typically filled in with zirconium.

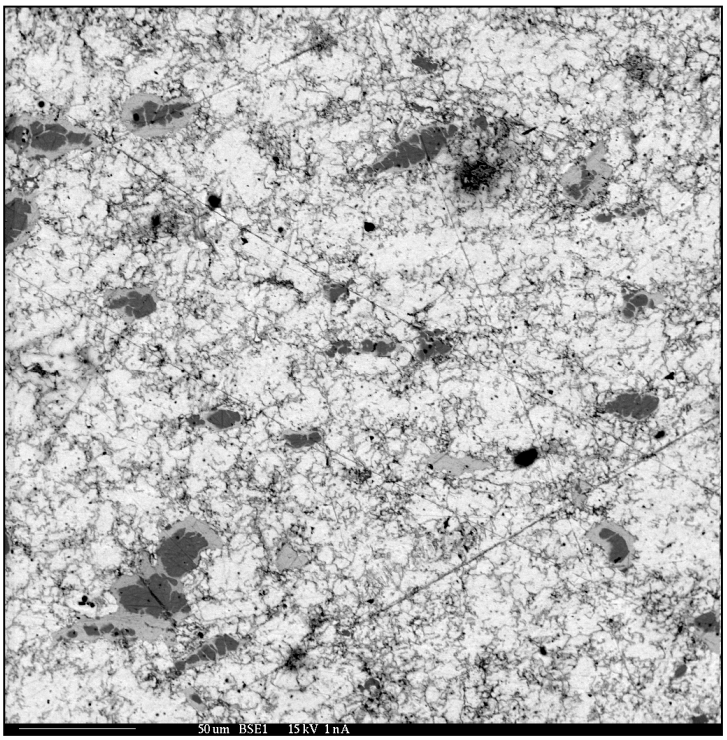

Figure 4-40: BSE image of Pellet 14 demonstrating low porosity.

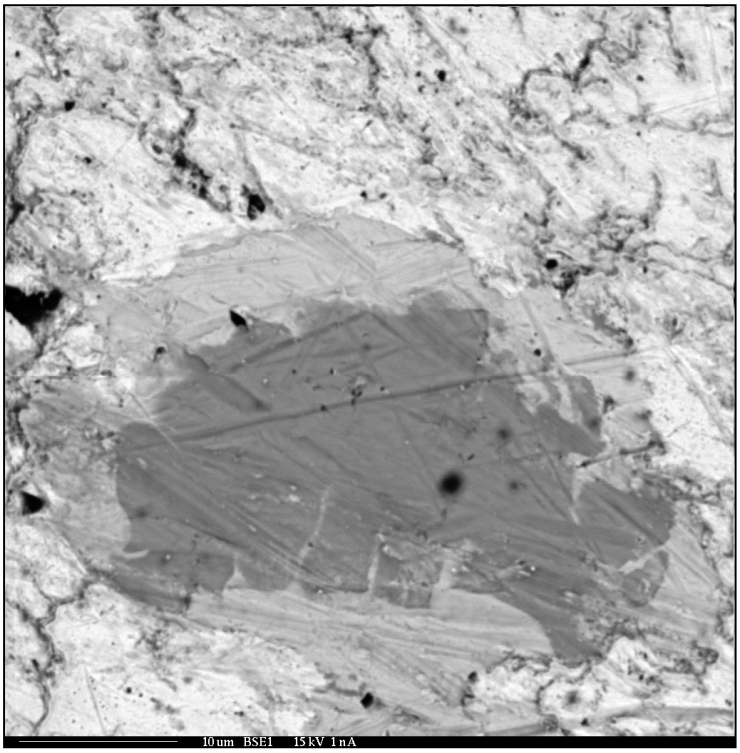

Figure 4-41 BSE image of Pellet 14 showing three region microstructure.

The final two DU-5Zr pellets were sintered using a novel technique involving cyclical transitions between the alpha and beta phases during sintering. The purpose of this method was to enhance sintering rate through the increase in atomic motion generated by phase changes. Pellet 15 was compacted with a pressure of 936 GPa. Pellet 15 was then sintered through ten alpha/beta phase transition cycles. In each cycle, the pellet was heated to the beta phase for approximately ten minutes, then cooled to the alpha phase for approximately twenty minutes. The shrinkage data acquired by LVDT is given in Figure 4-42.

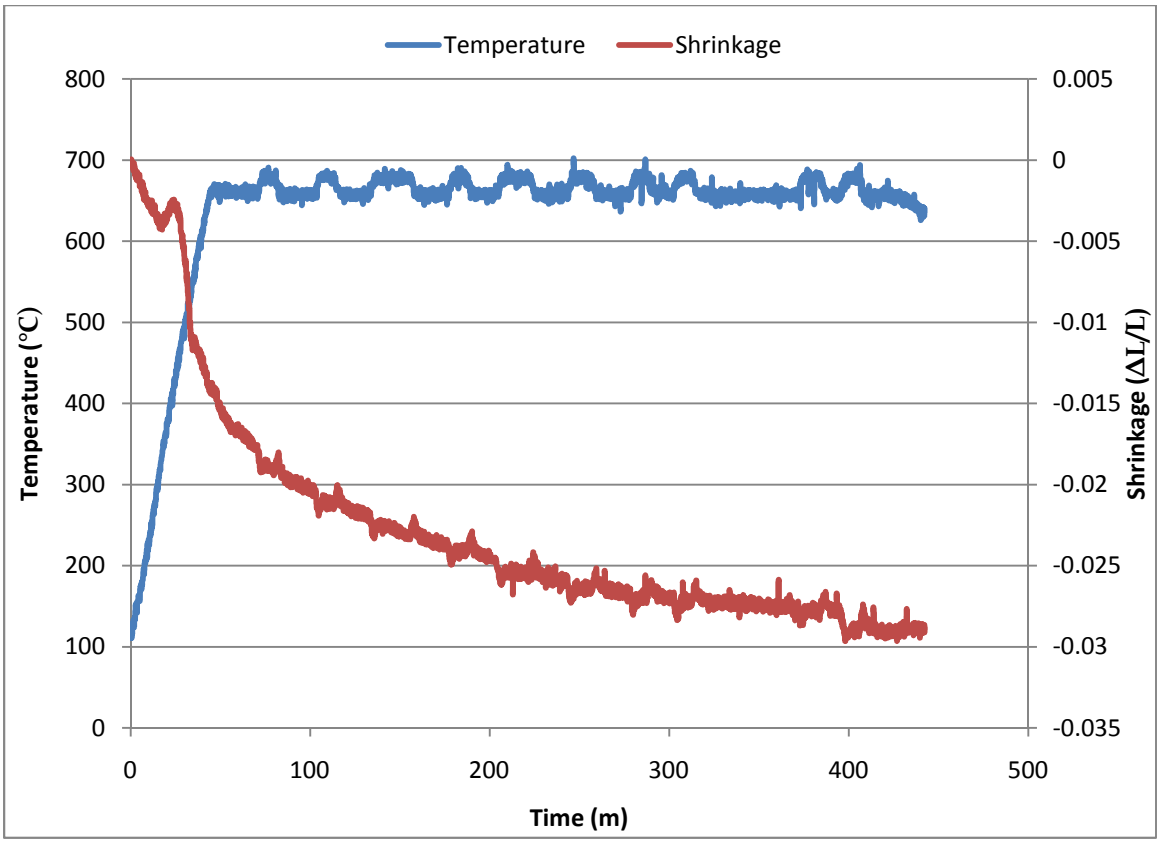

Figure 4-42: Shrinkage and temperature profile for Pellet 15.

As was done with other pellets, an attempt was made to section, polish, and image Pellet 15; however, Pellet 15 began to oxidize rapidly shortly following removal from the inert atmosphere of the glovebox. This oxidation was likely due to increased surface area from micro-cracks generated by density changes during phase transitions.

Pellet 16 was fabricated and sintered in a manner similar to Pellet 15, with the addition of a several hour period of isothermal alpha phase sintering following cyclical phase transition sintering. The purpose of this additional step was to reduce the micro-crack based surface area which was presumed to cause rapid oxidation in Pellet 15. The shrinkage and temperature data for Pellet 16 is given in Figure 4-43.

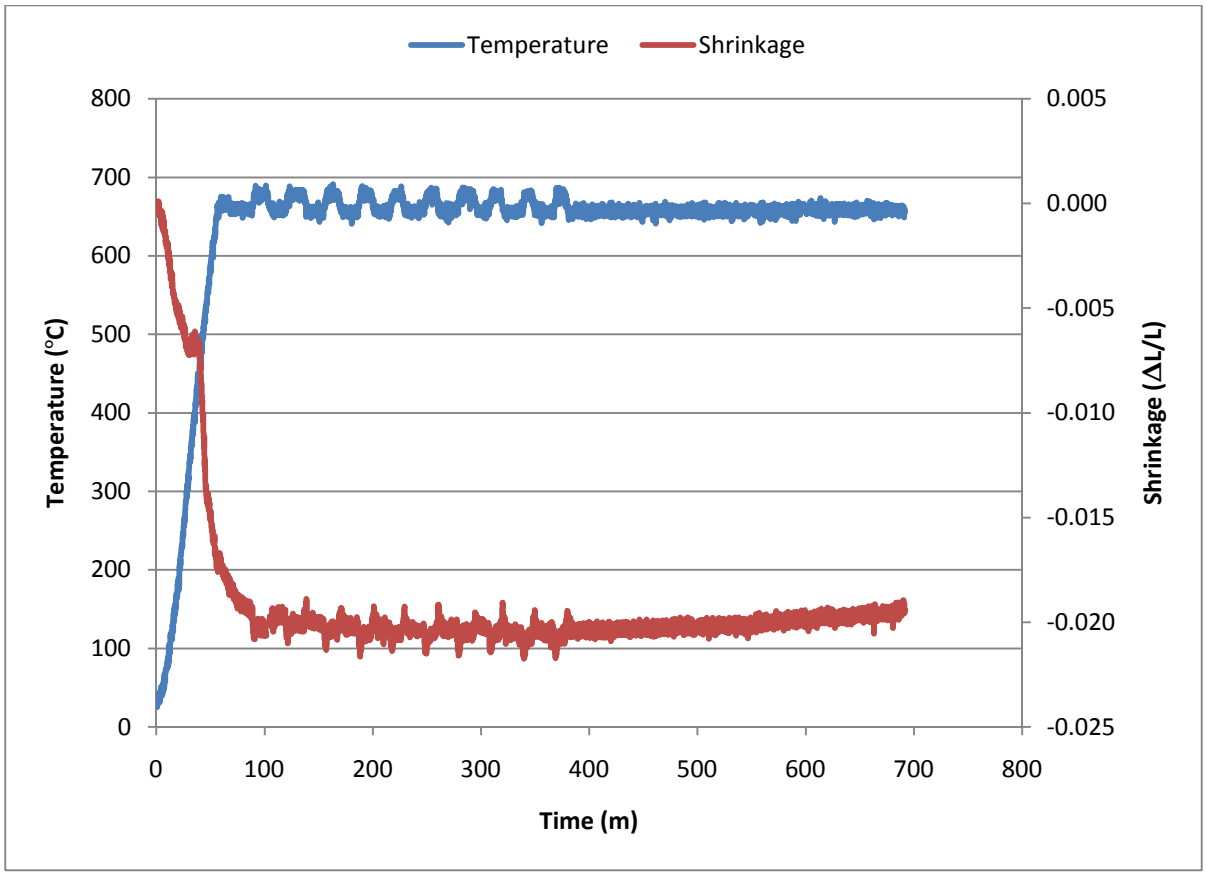

Figure 4-43: Shrinkage and temperature profile for Pellet 16.

Unlike Pellet 15, Pellet 16 did not rapidly oxidize following removal from an inert atmosphere, and thus it was sectioned, polished and imaged by SEM. Once again, porosity was consistent throughout the cross-section, with a calculated porosity from image analysis of 4.5%. The microstructure of Pellet 16 was similar to that of Pellet 14. The primary difference was in the composition of the boundary layer between the zirconium and uranium regions. The thickness of the boundary layer in Pellet 16 was smaller, on the order of only a few microns. In addition, the composition of the boundary region was higher in zirconium, with approximately 80a% Zr and 20a% U. Representative images of Pellet 16 showing these features are given in Figures 4-44 and 4-45.

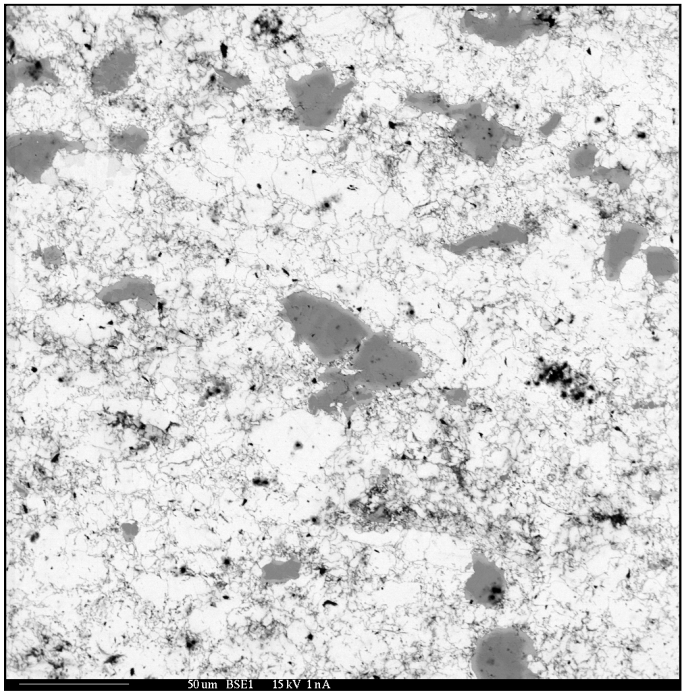

Figure 4-44: BSE image of Pellet 16.

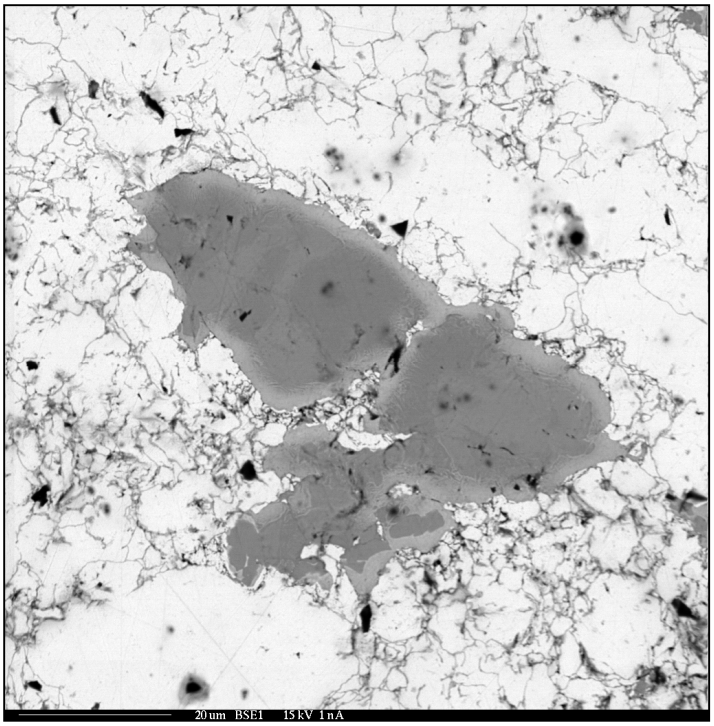

Figure 4-45: BSE image of Pellet 16 at higher magnification.

5. DISCUSSION

5.1 Uranium Powder Characterization

The size distribution (Fig. 4-2) and morphology (Fig. 4-1) of the uranium powder produced using the hydride/dehydride method were both consistent with expectations based on prior work and literature. The spalling process by which uranium hydride powder separates from bulk uranium produces fine powder with rough irregular shapes [16].

The average uranium particle size produced by the hydride/dehydride process is commonly noted in literature to be 40μm diameter [12,16]. This agrees well with the experimentally determined particle distribution in Fig. 4-2, which shows that the nominal particle size is very near to a particle diameter of 40μm. The shape of the distribution also corresponded well with expectations. The number distribution of particles peaked for very small diameter, then dropped with increasing size, while the volume distribution of particles follows a normal distribution with a long tail extending into the smaller particle region.

5.2 Uranium Sintering

An effect common to all sintered pellets, regardless of contents or processing conditions, was a dog-bone shaped region of increased density in the axial cross section of the pellet. This effect was a result of the pressing method used for pellet compaction. All pellets were fabricated using a dual-action punch and die. This method produces density gradients within the pellet, as shown in Figure 5-1. These gradients lead to slightly anisotropic sintering, making the sides of the pellet convex. This effect was also observable in post-sintering measurements of pellet diameter, as the top and bottom of each pellet were always slightly wider than the middle.

Electron microscope images, as shown in Figures 4-19 and 4-22 revealed a strong difference between the microstructures of the interior low porosity regions in the center of the pellets and the exterior high porosity regions of the pellets. In the high porosity region, necking and interparticle bonding is observed, but limited, and the original particles are still distinguishable. In the low porosity region, on the other hand, individual particles are no longer distinguishable, having sintered into a solid material with some remaining pores. This result indicates that the extra stress applied during compaction to the inner region directly resulted in better sintering, suggesting increased compaction pressure as a potential means to improve the quality of sintered pellets.

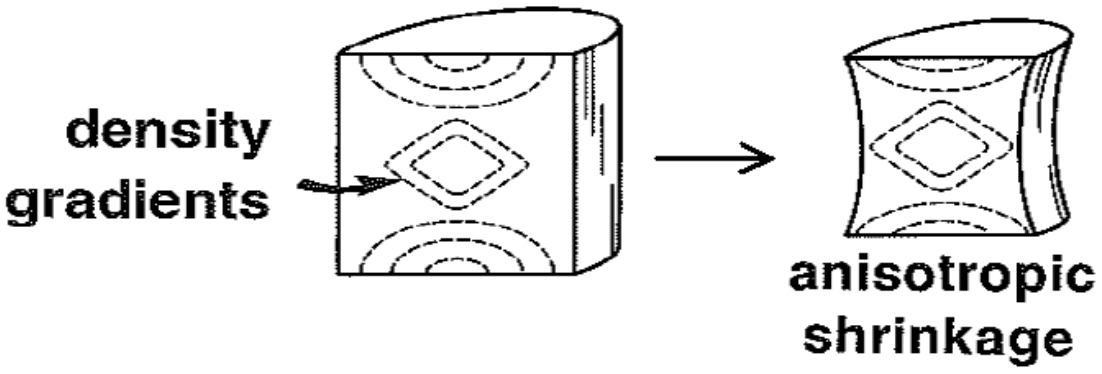

Figure 5-1: Density gradients and anisotropic sintering due to compaction method [4].

Another effect observed in many pellets was strong initial shrinkage during heating. The shrinkage typically began around 300ºC, lasting until the isothermal sintering temperature was reached. The two mechanisms which were initially thought to be responsible for this effect were sintering by plastic flow of dislocations, as described in Section 2.1.2 and removal of residual hydrogen gas from the hydride/dehydride process. It was found that increasing the duration of

the dehydriding step significantly reduced the degree of initial shrinkage, indicating that residual hydride decomposition was the most probable source of the majority of shrinkage during heating. The onset temperature for initial shrinkage of ~300°C agrees with this as well, since this is the temperature at which dehydriding become significant, and very little sintering would be expected at such a low temperature.

One of the issues encountered during previous work in alpha phase sintering of uranium and its alloys was widespread cracking due to delamination during the cooling phase following sintering. The severity of cracking ranged from moderate cracks a few millimeters in length to extended cracks across the full width of the pellets [3]. Analysis of previous results indicated that the probable causes of delamination were rapid cooling of the sample and poor control over the quality of the source powder used to fabricate the uranium pellets. Rapid cooling could potentially result in excess stress due to temperature gradients across the pellet, while the presence of large particles within the powder could result in localized areas with poor sintering which would be more susceptible to cracking. The lack of widespread delamination cracking in the sintered pellets from this research is attributed to 1) a uniform pressure distribution to minimize differentials in compaction stress across the pellet, 2) the sieving method used to remove large particles from the source uranium powder, and 3) the low controlled cooling rates used after sintering to minimize thermal stress. As shown in Figures 4-21, 4-22, and 4-23, the largest cracks were only a few hundred microns long, and most were only several microns in length.

5.2.1 Sintering of Uranium

Both the α-phase and γ-phase isothermal sintering curves were of the expected form, with initially rapid sintering gradually slowing as time passes. For each pellet, sintering in the γ-phase was significantly faster, as was expected due to the higher temperature and the higher diffusivity of uranium in the γ-phase [14].

Based on the sintering models described in Section 2.1.3, it was expected that log-log plots of sintering rate vs. time would be linear. Increases in isothermal sintering temperature were expected to shift the rate upwards (increase the y-intercept), while leaving the slope constant. These effects were generally observed, although Pellet 5 diverged from these expectations. In this case, the position of the log-log plot of sintering rate vs. time was lower than would be expected, based on the sintering temperature. In addition, the resulting slope varied slightly relative to the other experiments. The source of error for Pellet 5 may be related to the missing section of data from the experiment. Without this data, the true starting point for isothermal sintering may be slightly off.

The expected isothermal sintering mechanisms, as described in Section 2.1.2, were grain boundary diffusion and volume diffusion. Isothermal sintering by plastic flow occurs only in the presence of outside stress to generate dislocations, and surface transport mechanisms, such as evaporation-condensation and surface diffusion do not result in shrinkage, and would therefore not be measurable by the LVDT apparatus used in these experiments. Given the expectation of grain boundary diffusion and volume diffusion, the expected value of n was between five (volume diffusion) and six (grain boundary diffusion). The actual value of n would vary between these two values, depending on the relative contribution of each mechanism. However,

in the isothermal sintering experiments for pure DU, the average measured value of *n* was 3.92, excluding Pellet 5 and Pellet 7 for reasons discussed previously.

The discrepancy between the predicted and measured values of *n* is probably due to a combination of the morphology of the uranium powder and initial sintering contributions from plastic flow. The grain boundary diffusion and volume diffusion sintering models were based on the assumption of spherical particles; however, the uranium powder produced by the hydride/dehydride process was irregularly shaped. This deviation from the assumptions used by the sintering model may have resulted in a lower value of *n.*

The experimentally determined activation energy for alpha phase uranium sintering was 340 +/-41 kJ/mol. This value is significantly higher than the activation energy for gamma phase uranium sintering, which is 186.6 kJ/mol for the grain boundary diffusion mechanism [13]. This difference is consistent with previously made comparisons of diffusion in the alpha and gamma phases of uranium, which have concluded that diffusion in the alpha phase is far slower, requiring a greater activation energy.

5.2.2 Sintering of DU-10Zr

The isothermal sintering of U-10Zr was similar in several respects to the isothermal sintering of pure DU; however, some notable differences were observed. The most evident difference was the increased rate of isothermal sintering observed for U-10Zr, both for the α-phase and the γ-phase. Since the sintering process is driven by diffusion, the higher diffusivity of zirconium relative to uranium may be accredited for at least a portion of this increase in sintering rate. The mechanisms of two-component sintering may also contribute to the increased sintering rate of U-10Zr, due to activated sintering as zirconium accelerates the diffusion of uranium [4].

Interdiffuison between uranium and zirconium would be particularly active in the γ-phase, due to the high solubility of zirconium in γ-phase uranium.

In addition to increased sintering rate, the γ-phase sintering of U-10Zr demonstrated a a hump in shrinkage after several hours. It is likely that this shift was due to a transfer from the initial stage of sintering, which assumes point-contacts between particles, to the secondary stage of sintering, in which particles have densified to form an interconnected network. Once the initial phase of sintering formed sufficient connections between particles, interdiffusion and alloying of uranium and zirconium would become much more significant.

In similar fashion to pure DU sintering, the expected isothermal sintering mechanisms for U-10Zr were grain boundary diffusion and volume diffusion; however, the calculated values for *n* once again did not match with the predictions based on models of these mechanisms. This discrepancy was, as for pure DU, attributed to a combination of contributions from plastic flow and differences between the dendritic morphology of the uranium powder and the spherical particle assumptions employed by the sintering models. The average calculated value for *n* for α-phase sintering of U-10Zr was 2.65, compared to 3.92 for pure DU sintering. The lower value of *n* for U-10Zr may indicate a shift from grain boundary diffusion to volume diffusion, as sintering models predict a lower *n* for volume diffusion [4]. The lower value for *n* may also be an effect of sintering a mixture of powders, rather than a single powder, as the model used was developed for use with single powders.

In addition to the lower value of *n* observed for sintering of U-10Zr relative to DU, there was a difference in the calculated activation energy. The calculated activation energy for U-10Zr was 272 +/-91 kJ/mol, compared to a calculated value of 340 +/-41 kJ/mol for DU. When combined with the lower value of *n* observed for U-10Zr, this results in both faster sintering at a given

temperature and a higher sustained sintering rate over time relative to DU. The lower activation observed for U-10Zr is consistent with a shift from grain boundary diffusion to volume diffusion, based on activation energies for volume diffusion and grain boundary diffusion in gamma phase uranium. In the gamma phase, the activation energy of volume diffusion is lower than that of grain boundary diffusion. If the alpha phase of uranium behaves in a similar fashion, the lower activation energy for U-10Zr relative to DU may be caused by a zirconium driven shift to the volume diffusion mechanism. This would also be consistent with the lower value of *n* found for U-10Zr as previously discussed.

The uranium-zirconium microstructure as shown in Figures 4-37 and 4-38 contained three distinct regions. First, there were areas of pure zirconium within the sintered material. These regions were likely created by zirconium particles which did not fully diffuse into the uranium. Some of the pure zirconium regions included comb-like fingers extending into the uranium, indicating a partially completed diffusion process.

The second area observed is the lamellar structure containing significant amounts of both uranium and zirconium. The lamellar structure was found around the previously described pure zirconium regions. Quantitative analyses of the lamellar structure indicated an average smear composition of 41.3a% zirconium and 58.7a% uranium; however, the structure was too fine to allow quantitative analysis of the individual lamella. In spite of this, it may be reasonably surmised that the light gray portion of the lamellar structure is delta phase UZr_2, based on the much lighter shade of gray in this region relative to the regions of pure zirconium. Since the brightness of BSE images increases with atomic number, the lighter shade indicates the presence of a heavier material, such as uranium. This assumption is additionally validated by the smear

composition of the lamellar structure, which is approximately what would be expected if the light gray region were UZr_2 and there were equal amounts of both regions.

The final region of uranium-zirconium microstructure observed was the most prevalent, and consisted of sintered uranium with small spots of zirconium mixed throughout. This region had an average smear composition of 13.6a% zirconium and 86.4a% uranium. The amount of zirconium varied slightly throughout these regions; however, there were no areas of pure uranium found in the sintered samples.

5.2.3 Sintering of DU-5Zr

The primary goal for Pellet 14 was to demonstrate the feasibility of an exclusively alpha-phase sintering process for pellet fabrication. The compaction pressure was doubled from that used previously in an effort to remove the outer low-porosity region observed previously. Based on SEM imaging of Pellet 14, this increase was effective, as consistently low porosity was observed throughout the full cross-section of Pellet 14. This consistency would be ideal for fabrication of nuclear fuel.

The cyclical phase transition sintering technique used for Pellets 15 and 16 was designed to increase the rate of sintering by increasing atomic motion and diffusion. This method produced mixed results, as greatly enhanced sintering was observed in Pellet 15, but not in Pellet 16. It is unknown why this difference occurred, as very similar processing techniques were used for both pellets. Further studies of cyclical sintering for DU-Zr should be performed to determine if the increased sintering rate observed in Pellet 15 may be consistently reproduced.

One of the expected side effects of cyclical phase transition sintering was an increase in porosity due to repeated density changes during phase transitions. The porosity observed for

Pellet 16 was slightly higher than the porosity previously observed for isothermally sintered DU-Zr pellets, indicating that a degree increased porosity may have occurred due to repeated phase changes. However, the sintering time for Pellet 16 was significantly lower than that of isothermally sintered DU-Zr pellets, which may have contributed to the slightly increased porosity.

Pellets 14 and 16 were both sintered without reaching the gamma phase, which resulted in a slightly different final microstructure. Previous DU-Zr pellets which had been sintered partially in the gamma phase produced a lamellar α+δ microstructure in some regions as shown in Figure 4-39. In Pellets 14 and 16, on the other hand, no lamellar region was observed. In Pellet 14, an equilibrium UZr_2 phase was observed, as shown in Figure 4-41. The presence of this phase indicates inter-diffusion of uranium and zirconium during sintering. Further studies varying the sintering time may be useful in determining the rate of diffusion based on the thickness of the UZr_2 region.

The uranium-zirconium phase in Pellet 16, shown in Figure 4-45, was slightly different, as quantitative analysis showed greater zirconium concentration than would be expected for UZr_2. This result may be explained by the fact that the sintering time for Pellet 16 was approximately one fourth of the sintering time for Pellet 14. The shorter time period for diffusion likely resulted in the formation of a non-equilibrium UZr_2+Zr phase. Since this phase contained excess zirconium, it may be concluded that inter-diffusion occurs by diffusion of uranium into zirconium. As the diffusion time increases, the uranium content would increase, eventually resulting in the formation of the equilibrium UZr_2 phase observed in Pellet 14.

6. SUMMARY

The alpha phase sintering of uranium and uranium-zirconium were successfully characterized in this research. These results provide the scientific background necessary to demonstrate the feasibility of a low temperature powder metallurgy process for the fabrication of metal uranium fuel. A summary of the primary conclusions are as follows:

1. A model for the initial phase of sintering for uranium and uranium-zirconium was evaluated based on isothermal shrinkage rates during sintering. Based on the model the activation energy for sintering DU and DU-10Zr in the alpha phase were found to be 340 +/-41 kJ/mol and 272 +/-91 kJ/mol respectively.
2. The effects of zirconium addition to uranium during sintering were analyzed and the resulting pellets were compared to those composed exclusively of uranium. It was found that the addition of zirconium accelerated sintering due to uranium-zirconium inderdiffusion.
3. The microstructure of sintered uranium-zirconium pellets was analyzed, indicating the presence of the alloyed alpha+delta phase when sintered in the gamma phase, and the presence of the alloyed delta phase when sintered in the alpha phase. This result was attributed to the relative solubility of zirconium in the uranium gamma and alpha phases.
4. The previously developed hydride/dehydride process for powder production was vastly improved to increase the volume of powder produced, and the uranium powder produced by this method was characterized to determine size distribution and morphology.

5. Previous issues with pellet cracking during cooling due to delamination were resolved by the use of controlled cooling and finer control over the quality of the uranium powder used.

If further research is undertaken in this area, the following recommendations are made:

1. The sintering models produced should be expanded by the use of further uranium-zirconium compositions and small amounts of secondary elements to represent transuranics.
2. The effects of pressure-assisted sintering should be analyzed to increase the rate and quality of sintering.
3. Possible applications for the fabrication of metal fuel with low smear density utilizing the low temperature sintering techniques developed in this thesis should be investigated.

REFERENCES

1. D. E. Burkes, R.S. Fielding, and D.L. Porter, Metallic Fast Reactor Fuel Fabrication for the Global Nuclear Energy Partnership, Journal of Nuclear Materials 392 (2009), 158-163.
2. C.L. Trybus, J.E. Sanecki, S.P. Henslee, Casting of Metallic Fuel Containing Minor Actinide Additions, Journal of Nuclear Materials 204 (1993) 50-55.
3. D. Garnetti, S.M. McDeavitt, Uranium Powder Production via Hydride Formation and Alpha Phase Sintering of Uranium and Uranium-Zirconium Alloys for Advanced Nuclear Fuel Applications. Masters Thesis, Texas A&M University, College Station, TX.
4. J.J. Carroll, A.J. Melmed, Field Ion Microscopy of Alpha Uranium, Surface Science 116 (1982) 225-239.
5. W.D. Wilkinson, Uranium Metallurgy, John Wiley & Sons, Inc., New York (1962).
6. L. Grainger, Uranium and Thorium, George Newnes Limited, London (1958).
7. S.F. Pugh, Swelling in Alpha Uranium due to Irradiation, Journal of Nuclear Materials 4 (2) (1961) 177-199.
8. J.J. Burke, D.A. Colling, A.E. Gorum, J. Greenspan, Physical Metallurgy of Uranium Alloys, Brook Hill Publishing Company, Columbus, Ohio(1976).
9. C.E. Stevenson, The EBR-II Fuel Cycle Story, American Nuclear Society Inc. La Grange Park, Illinois (1987).
10. S.M. McDeavitt, A.A. Solomon, Hot-Isostatic Pressing of DU-10Zr by a Coupled Grain Boundary Diffusion and Creep Cavitation Mechanism, Journal of Nuclear Materials 228 (1996) 184-200.
11. P. Chiotti, B.A. Rogers (1950), The Production of Uranium and Thorium in Powder Form, United States Atomic Energy Commission, AECD-2974.

12. S.M. McDeavitt (1992), Hot Isostatic Pressing of DU-10Zr Alloy Nuclear Fuel by Coupled Grain boundary Diffusion and Power-Law Creep. Ph.D Thesis, Purdue University, West Lafayette, IN.

13. R.M. German, Sintering Theory and Practice, John-Wiley & Sons, Inc., New York, (1996).

14. F.V. Lenel, Powder Metallurgy, Metal Powder Industry, (1980).

15. T. Hashino, Y. Okijima, Mechanism of the Reaction of Hydrogen with Uranium, Journal of Physical Chemistry 77 (1973) 2236-2241.

16. C.R. Clark, M.K. Meyer, Fuel Powder Production from Ductile Uranium Alloys, Presented at the 1998 International Meeting on Reduced Enrichment for Research and Test Reactors, Oct. 18 - 23, 1998, Sao Paulo, Brazil.

17. J. Bloch, The Hydriding Kinetics of Activated Uranium Powder Under Low (Near Equilibrium) Hydrogen Pressure, Journal of Alloys and Compounds 361 (2003) 130–137.

VITA

Grant William Helmreich received his Bachelor of Science degree in Nuclear Engineering and his Bachelor of Arts degree in Chemistry from Texas A&M University in 2009. He then received a Masters of Science in Nuclear Engineering at Texas A&M University in December 2010. His research interests include the fabrication and testing of advanced nuclear fuels, particularly metal fuels.

Grant William Helmreich may be reached at Dept of Nuclear Engineering, Texas A&M University, College Station, TX 77843-3133. His email is granthelmreich@gmail.com.